Materials Chemistry and Physics 282 (2022) 125881

Contents lists available at ScienceDirect

Materials Chemistry and Physics

journal homepage: www.elsevier.com/locate/matchemphys

Nanostructured P-doped activated carbon with improved mesoporous texture derived from biomass for enhanced adsorption of industrial cationic dye contaminants

Kamal M.S. Khalil[a,*], Walaa A. Elhamdy[a], Khaled M.H. Mohammed[a], Abd El-Aziz A. Said[b]

[a] Chemistry Department, Faculty of Science, Sohag University, P.O. Box 82524, Sohag, Egypt
[b] Chemistry Department, Faculty of Science, Assiut University, P.O. Box 71516, Assiut, Egypt

HIGHLIGHTS

- P-doped activated carbon ACP adsorbents were derived from orange peel residues.
- ACPs were nanostructured into amorphous graphite nanoparticles of few graphene layers.
- ACP adsorbents showed high surface up to 1700 m^2/g with improved mesoporosity >90%.
- ACPs showed remarkable adsorption capacity (452 mg/g) for methylene blue (MB) dye.

GRAPHICAL ABSTRACT

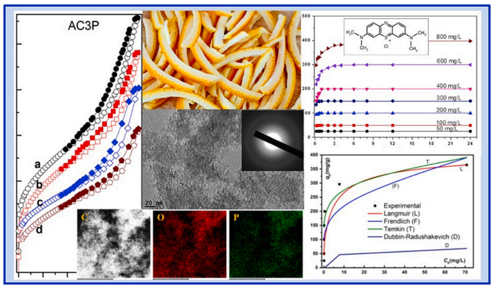

ARTICLE INFO

Keywords:
Nanoporous
Carbonaceous material
Graphene-like
HRTEM
Methylene blue
Activated carbon

ABSTRACT

Developing of high-performance carbonaceous materials from biomass is a significant contemporary research subject to meet the increasing demand for functional adsorbents with low price, high available and sustainability for adsorptive removal processes of industrial pollutants. The present work investigates formation of nanostructured surface modified P-doped activated carbon (ACP) materials via thermochemical activation of orange peel (OP) biomass residual materials, by phosphoric acid, H_3PO_4. Different impregnation ratios of phosphoric acid to OP (w/w) were investigated at different activation temperatures (400–800 °C). The formed ACP materials were characterized by TGA−DTA, FTIR−ATR, Raman spectroscopy, XRD, N_2 gas adsorption/desorption, HR−TEM microscopy, EDX and elemental surface mapping. The results indicated that ACP materials were structured in the form of plate-like nanoparticles of amorphous graphite that composed of few graphene layers. The ACP materials exhibited high surface area (up to 1700 m^2/g) with high contribution from mesoporosity (up to 94%) of slit-like pore shape. The point of zero charge was found at pH of 6.3, which permits application at neutral adsorption conditions. The formed ACP adsorbents exhibited distinguished adsorption capacities, q_{ads}, for methylene blue (MB) with successful recyclability. The adsorption capacities were enhanced (up to $q_{ads} = 452$ mg/g) for the materials formed at high acid impregnation ration and activated at high temperatures. The adsorption process of MB was spontaneous, fits with the Langmuir adsorption isotherm and pseudo-second-order kinetic. The high adsorption capacities for the ACP adsorbents were correlated with their micro/nano-structures, which were dominated by nano plate−like amorphous graphite particles composed of few graphene−like layers.

---

* Corresponding author.
E-mail addresses: kms_khalil@yahoo.co.uk, kms_khalil@science.sohag.edu.eg (K.M.S. Khalil).

https://doi.org/10.1016/j.matchemphys.2022.125881
Received 3 October 2021; Received in revised form 25 January 2022; Accepted 15 February 2022

1. Introduction

Nanotechnology drives the recent development of novel nanomaterials for acting as adsorbents for different pollutants with high adsorption capacity and selectivity [1]. Biomass-derived porous carbon materials have recently received extensive attention as high-performance sustainable adsorbents due to their high surface area, developed porous texture and graphitic−like structure [2], [3]. Organic molecules discarded by industrial effluents from many manufacturing processes, such as textile, paper, drug, pulp, plastic, and printing are hard to damage when discharged into water due their high resistant to light and oxidizing agents [4,5]. Thus, a variety of techniques are available for dyes and organic molecules removal, which includes ultrafiltration, ozonation, oxidation, flocculation and adsorption. However, adsorption is an effective technique for dye removal, due to the low operational cost and high removal efficiency [6]. Methylene blue (MB) has a wide range of industrial applications as a dye for paper, cotton, wools, hair and many other applications. Moreover, MB dye frequently employs as a model adsorbate molecule to study the separation of colored dye species and colorless organic molecules from various contaminated mixtures [7].

Different types of carbonaceous adsorbents can be derived from Lignocellulose biomass materials. Thus, the native biomass form of fruit shells, husks, cactus barks, leaves have been utilized for dye removal process [8], [9]. Moreover, many activated carbons adsorbents have been obtained by thermodchemical activation of banana trunk [7], sorghum stalk [3], banana biochar [10] almond shell [11], peanut hulls [12,13], sugarcane bagasse [14], pineapple peel [15] and date palm pits [16]. More recently, conversion of biomass materials into carbon nanotube [6], and graphene-like porous carbon nanostructure [17] for efficient adsorption of organic dyes have been investigated. Thus, the main advantages of utilization of renewable biomass derived carbonaceous materials includes: availability, low cost, eco-friendly nature and surface texture tune−ability [18].

There are many thermochemical activation reagents for the conversion of biomass into activated carbon (e.g. inorganic acids, metal salts and alkalis) [19]. However, the utilization of phosphoric acid, H_3PO_4, as an activation reagents, is very interesting in particular because it leads to higher carbon yield, high thermal/chemical stability, and has ecofriendly properties. Phosphoric acid plays many other roles during thermochemical activation process, especially as a phosphorous (P) dopant. Doping of P largely improves surface properties, modulates the electronic structure and provides more active sits ready for adsorption [20]. Moreover, H_3PO_4, reduces the formation of surface carbon-oxygen groups of quinone, (C═O); phenol, (C–OH); carboxylic, (-COOH); ether, (C–O–C) groups; and replaces them by different C–O–P type of groups, such as $(CO)_3PO$ and $(CO)_2PO_2$; $C\text{-}O\text{-}PO_3$; and $C_2\text{-}PO_2$ type of groups [21], [22]. Thereby, insertion of P stabilizes the involved carbonaceous materials against oxidation at high temperatures.

Biomass-derived carbon materials from orange peel (OP), have been recently stimulated the interest of many investigators for applications as adsorbents [23–27], electrode materials [28,29] and super capacitor [30–32]. However, the above indicated materials were either of low surface area or suffer from low ratio of mesoporosity [30–32]. However, the characteristic of the biomass derived carbonaceous materials are controlled by two groups of factors. The first group is related to pyrolysis conditions, and the second is inseparably linked with raw material properties and biomass characteristics [33]. Orange peel (OP) is a soft lignocellulose material that mainly composed of cellulose, hemicelluloses, lignin, pectin and chlorophyll pigments and can be converted into carbonaceous materails. Therefore, it is important to investigate micro/nano−structure of the OP derived carbonaceous materials, which is controlled by the precursor composition. Given that the Global annual production of OP has been estimated to > 60 million tons of orange fruits [34]. Thus, it is important to consider valorization of the associated large amounts of the orange peels. Moreover, orange production represents around 65% of total citrus fruits productions and about 30% of total fruit production in Egypt. Orange production in Egypt enjoys variety of orange types, among these types “Navel oranges” considers as Egypt’s top export accounting for 60% of total orange production [35].

The present work investigates the formation and utilization of P-doped activated carbon (ACP) materials from OP in an effort for valorization of such sustainable, agro-industrial biomass material. Recently, we have managed formation of efficient group of adsorbents for Cr(VI) anions from solutions [34], as well as ACP catalyst and support for WO_3/ACP catalysts from OP [36]. The present work aims investigation of surface texture and micro/nano structural characteristics of the OP−derived carbonaceous materials, which termed as ACP. The ACP materials were produced at different phosphoric acid to OP (w/w) rations and activated at different temperatures up to 800 °C. Moreover, the work investigates utilization of the formed ACP materials as adsorbents towards batch adsorption of methylene blue (MB), as a model organic/colored dye adsorbate. The adsorption kinetics and thermodynamics were investigated and analyzed to learn about the physicochemical surface properties of the adsorption process. The adsorption performances of the ACP materials were interpreted in terms of their surface textures and nanostructures.

2. Materials and methods

2.1. Materials

Orange peel (OP) was collected on the midseason time from washed oranges, Navel type grown in Egypt, as fruit reside. The orange peels were cut into small pieces, left to dry in air for a few days and drying further in a drying furnace at 110 °C for an overnight. The dried OP material was stored and used as a stock.

Chemicals including phosphoric acid, H_3PO_4 (85%), specific gravity of 1.69 g/mL; hydrochloric acid (HCl, 36%) and sodium hydroxide (NaOH, 98%), ethanol (99.5%), HNO_3 (70%) were products of Adwic (Egypt). Methylene bule, $C_{16}H_{18}ClN_3S$ (MW = 319.85 g/mol, $pKa = 5.6$, and $\lambda_{max} = 664$ nm) was product of Merck (Germany).

2.2. Formation of P-doped activated carbon

The ACP materials were formed by a thermochemical activation method involving phosphoric acid, H3PO4, as an activation reagent and P-doping source [34,36]. Portions of dry orange peel (OP) were impregnated with H3PO4: OP ratios as 1: 2; 1: 1; and 2: 1 (w/w). The mixtures were kept at 110 °C for 24 h to initiate dehydration by H3PO4, followed by thermal treatment in a Muffle furnace at ramp rate (10 °C/min) in a flow of N2 gas (150 mL/min) up to one of the targeted activation temperature (400, 500, 600 or 800 °C) for 60 min. After this, the activated materials were allowed for cooling to the room temperature inside the Muffle furnace under the flow of N2 gas. The pyrolysis products were washed (and filtered) many times with hot and cold distilled water until pH value of the filtrates reach 6.5. The formed materials were dried at 120 °C in a drying furnace for an overnight. The activated carbon thus obtained with different ratios of phosphoric acid: OP (1:2, 1:1, and 2:1) were termed as AC1P, AC2P, and AC3P, respectively. The thermal activation products were named after their activation temperatures (400, 500, 600 or 800 °C), respectively. For example, AC1P400 indicates ACP materials obtained at the first phosphoric acid: OP ratio (1:2) and thermally activated at 400 °C. Table 1 summarizes the preparation parameters and the relative code name given for each produced materials.

2.3. Characterization techniques

Carbon, hydrogen and nitrogen (C, H, and N) contents in the formed materials were determined by a Vario-EL elemental analyzer. XRD characterization was performed utilizing a Model Bruker D8 ADVANCE

Table 1
The code names, formation parameters and formation yields of the formed ACP materials.

Code Name	H_3PO_4: OP(dry)	Activation Temperature	Formation yield
AC1P400	1: 2	400	40.0
AC2P400	1: 1	400	40.4
AC3P400	2: 1	400	42.5
AC1P500	1: 2	500	39.8
AC2P500	1: 1	500	40.1
AC3P500	2: 1	500	41.9
AC1P600	1: 2	600	37.0
AC2P600	1: 1	600	39.8
AC3P600	2: 1	600	39.5
AC1P800	1: 2	800	34.8
AC2P800	1: 1	800	33.5
AC3P800	2: 1	800	31.8

X-ray diffractometer, at Cu $K\alpha$ radiation ($\lambda = 1.540$ Å). Identifying the surface functional groups in the ACP adsorbent and/or the adsorbate MB species were characterized by the FTIR analysis in the attenuated total reflectance (ATR) mode using a model 6700 Nicollet spectrophotometer (USA), where the spectra were recorded in the region of 4000–400 cm^{-1}. Raman spectra of the materials were obtained using a Raman spectroscopy instrument model Senterra Inverted Configuration (Germany) under ambient condition. A 785 nm laser was used as the exciting source on the sample surface with a power of 50 mW. Simultaneous (TG−DTA) analyses were carried out using a Shimadzu Thermal Analyzer; model TGA-60H (Japan). The analyses were carried out simultaneously upon heating up to 1000 °C at a ramp rate of 10 °C/min, under a flow of nitrogen gas or air of 30 mL/min. Transmission Electron Microscopy was performed by a model JEOLJEM-2100F electron microscope linked with an energy dispersion medium unite model (EDS Oxford instrument X-MAX,80mm2). Nitrogen adsorption/desorption measurements were carried out using a Micrometrics Instrument model ASAP 2010 (U.S.A.) at −196 °C. Prior to analysis, the samples were degased at 300 °C under vacuum condition (<1 Pa) for 3 h. The adsorption data were processed by the instrument software to obtain the specific surface area by BET equation, S_{BET}. Micropore surface area (S_{mic}) and external surface area (S_{Ext}) of the ACPs materials were determined via the *t*-plot method using Halsey equation. Total pore volume V_T was calculated at $p/p^o = 0.95$. Pore width distributions were calculated by the BET (P_{BET}) and BJH (P_{BJH}) methods.

2.4. Adsorption study

2.4.1. Adsorption measurements

2.4.1.1. Empirical adsorption equilibrium. Empirical adsorption equilibrium study was performed in a set of 100 ml glass bottles under the selected conditions of temperature = 25 ± 1 °C; ACP adsorbent mass = 100 mg/50 mL (MB solution); and pH = 6.5. Different MB concentrations (50–800 mg/L) were employed to investigate the effect of MB initial concentration. All batch adsorption experiments were made using an orbital shaker (Dragon Lab model SK-0330-pro) operated at 150 rpm and equipped with an air thermostatic cabinet controlled by a digital controller (model MC810, Electrothermal, England). The equilibrium concentration of MB solution was measured in the filtrate solution using a double beam UV–vis spectrophotometer (PgT80) at 664 nm. The amount of adsorption at equilibrium, q_e (mg/g) and percentage removal were calculated by Eq. (1) and Eq. (2), respectively:

$$q_{e=\frac{(C_o - C_e)}{m}V} \quad (1)$$

$$\text{Removal} \quad \% = \frac{c_o - c_e}{c_o} \times 100 \quad (2)$$

where C_0 and C_e (mg/L) represent the initial and the equilibrium MB concentrations, *V* represents solution volume (L) and *m* represents the adsorbent mass (g). The obtained empirical adsorption results were linearly as well as nonlinearly fitted with the examined adsorption isotherm models as shown below.

2.4.2. Point of zero charge

Measurement of the point of zero charge, pH_{PZC}, was performed for the test ACP material as described [37]. A mass of 0.025 g of solid test material was placed in contact with 25 mL of aqueous solution under different conditions of initial (pH = 2–12). The initial pH values were adjusting by addition of 0.1 M of NaOH or HCl solution. The mixtures were subjected for stirring in an air thermo-stated orbital shaker operated at 150 rpm for 24 h at 25 ± 1 °C. Then, the final pH of each solution was measured. The values of ΔpH change against the initial pH values were graphically represented.

2.4.3. Effect of the initial solution pH on MB adsorption

Effect of the initial solution pH on the adsorption of MB (q_{ads}, mg/g) and the removal (%) of MB on the test ACP material was investigated for different initial pH values (2.0–12.0). The experiments were performed under fixed conditions of initial MB concentration (100 mg/L), carbon dose (0.100 g/50 mL), stirring rate (150 rpm), contact time (3 h) and constant temperature (25 ± 1 °C).

2.4.4. Kinetic measurements

The kinetic investigation was carried in a set of 100 mL glass bottles in a procedure similar to the above equilibrium measurements at the following conditions of (temperature = 25 ± 1 °C; adsorbent mass = 100 mg/50 mL (MB solution); pH = 6.5, and [MB] = 50–800 mg/L).

The charged bottles were mounted on the air thermo-stated orbital shaker, which was operated at 150 rpm, 25 ± 1 °C and left shaking up to 24 h (where no further kinetic change were observed). Small portions of the solution were withdrawn at successive time intervals and concentrations of MB were measured as above. The MB concentration was calculated at any time (*t*), as q_t (mg/g) by:

$$q_{t=\frac{(C_o - C_t)}{m}V} \quad (3)$$

where C_0 and C_t (mg/L) represent the initial and any time (*t*) MB concentrations, *V* is the solution volume (L) and m is the ACP adsorbent mass (g). The obtained empirical adsorption results were linearly and nonlinearly fitted with the examined kinetic models. Namely, the pseudo-first-order [38], pseudo-second-order [39], and intra−particle models [40] kinetic models to evaluate the kinetic parameters.

2.5. Effect of temperature on MB dye adsorption

The effect of temperature of MB adsorbate solution was investigated on the AC3P800 at different temperature (298, 303, 308, 313 and 318 ± 1 K) for different initial concentrations (200, 300 and 400 mg/L) of MB solution using a fixed dose of ACP adsorbent (100 mg/50 mL). From the thermal interaction results different thermodynamic parameters were determined by employing of Van't Hoff equation. The standard Gibbs free energy change ($\Delta G°$), standard enthalpy change ($\Delta H°$) and standard entropy change ($\Delta S°$) were estimated in terms of Eqs. (4) and (5). Surface coverage (θ) was calculated from Eq. (6), the activation energy (E_a) and sticking probability (S^*) were estimated in terms of Eq. (7) as given below.

$$\ln K_c = \frac{\Delta S°}{R} - \frac{\Delta H°}{R}\left(\frac{1}{T}\right) \quad (4)$$

$$\Delta G^{\circ} = \Delta H^{\circ} - T\Delta S^{\circ} \tag{5}$$

$$\theta = \left(1 - \frac{C_e}{C_o}\right) \tag{6}$$

$$S^{*} = (1-\theta)e^{\frac{-E_a}{RT}} \tag{7}$$

2.6. *Desorption and regeneration studies*

Desorption study was performed with the ACP adsorbent saturated with adsorbed MB as follows. A given adsorbent amount (100 mg) was added to a solution containing 50 mL of 100 mg/L MB. The mixture was mounted on an orbital shaker (150 rpm) for 3 h at 25±1 °C, and the amount adsorbed (q_{ads} mg/g) was determined. Different eluents were investigated for desorption of MB (absolute ethanol; HCl (1 mol/L); absolute ethanol + HCl (1 mol/L), 9:1, (v/v) ratio, HNO3 (1 mol/L), and NaOH (1 mol/L) solutions. The most efficient eluent, (absolute ethanol + HCl (1 mol/L), 9: 1 (volume ratio) was employed.

The solid adsorbent was filtered off quantitatively and treated with 20 mL portion of the elution solvent solution, respectively, stirred for 60 min at 30±1 °C to accelerate desorption of the adsorbed MB [41]. The mixture was filtrated and the eluent containing desorbed MB was collected. Then, the regenerated adsorbent was dried at 110 °C, weighed and subjected to the next adsorption/desorption cycle.

The desorption procedure was repeated many times with a fresh portions of the eluent till all MB molecules were desorbed (no more MB was recognized) and all the filtrates were collected together. The collected desorption filtrates was adjusted to a fixed volume. The total amount of MB recovered from the sample (q_{des}, mg) during the desorption cycles was measured. The desorption (%) of MB for the adsorption/desorption cycle was calculated as:

$$Desorption\ (\%) = \frac{qdes}{qads} \times 100 \tag{8}$$

Then, the regenerated adsorbent was dried at 110 °C, weighed and subjected to the next adsorption/desorption cycle. The recycling experiments were carried out four times.

3. Results and discussion

3.1. *Formation yield and elemental analysis*

The formation yield for the different ACP materials are shown in Table 1. Formation yield values of 40.0, 40.4 and 42.5% were obtained for AC1P400, AC2P400 and AC3P400, respectively. The yield values were slightly decreased with increasing of the activation temperatures to 500 and 600 °C. However, reasonably high yield values of 34.8, 33.5 and 31.8 were preserved for AC1P800, AC2P800 and AC3P800, respectively. Thus, the formation yields were decreased with increasing of the activation temperature. This also indicates that larger amount of volatiles gases were evolved (equals weight loss) during activation at higher temperatures. Weight loss (100 – yield%) during the thermochemical activation process of the biomass material depends mainly on the amount of carbon removed by interacting with O and H atoms in the form of evolved gases (e.g. CO, CO_2, H_2O, CH_4) or tar [42]. The high formation yield values were due to the utilization of phosphoric acid as activation reagent, which enhanced the dehydration, polymerization, restructuring of constituent biopolymers and favors the conversion of aliphatic to aromatic compounds [43].

Elemental analysis of the produced materials, Table S1 (Electronic Supplementary Materials) showed that carbon (C) contents were increased (from 76 to 86%) on going from AC1P800 to AC3P800, and were increased (from 78 to 86%) on going from AC3P400 to AC3P800. This indicates that carbon contents were increased with increasing of the impregnation ratio (H_3PO_4:OP) and with increasing of the activation temperature. Moreover, the amount of hydrogen (H) contents was also decreased with increasing of the activation temperature, which indicates progressive aromatic condensation process [44].

3.2. *Structural characterization*

3.2.1. *XRD diffractometery*

XRD patterns for the AC1P, AC2P and AC3P group of materials, which were activated at different temperatures (400–800 °C) are shown in Fig. 1 (A, B and C), respectively. The patterns showed clear broad peaks around $2\theta = 24.2°$ and 43.13°, which are due to the (002) and (101) crystal planes of amorphous graphite structure (File No., 75–1621) [35,36,45]. On moving from AC1P to AC2P to AC3P and with increasing of activation temperature, Fig. 1, the intensity of the peak 24.2° was decreased and a new peak at 13.13 was increased. The latter peak corresponds to (001) crystal plane of graphite oxide structure [46–48]. This indicates that surface oxidation process was occurred for the graphite layers at higher activation temperatures, specially, for the materials obtained with high acid impregnation ratios (AC3P600 and AC3P800). It is clear that the intensity of the graphite oxide peak was in the order of AC3P400 < AC3P500 < AC3P600 < AC3P800 i.e. increases with increasing of the acid ration. This confirms the direct effect of phosphoric acid on the formation of the graphite oxide peak. XRD patterns for the dried OP precursor and a standard graphite sample are presented in Fig. S1, for comparison. The OP sample showed amorphous nature, whereas a of graphite sample showed the crystalline structure of graphite (File No., 75–1621).

Particle size determination were performed via Scherer's equation from the broad diffraction (002) peaks and resulted in values within the

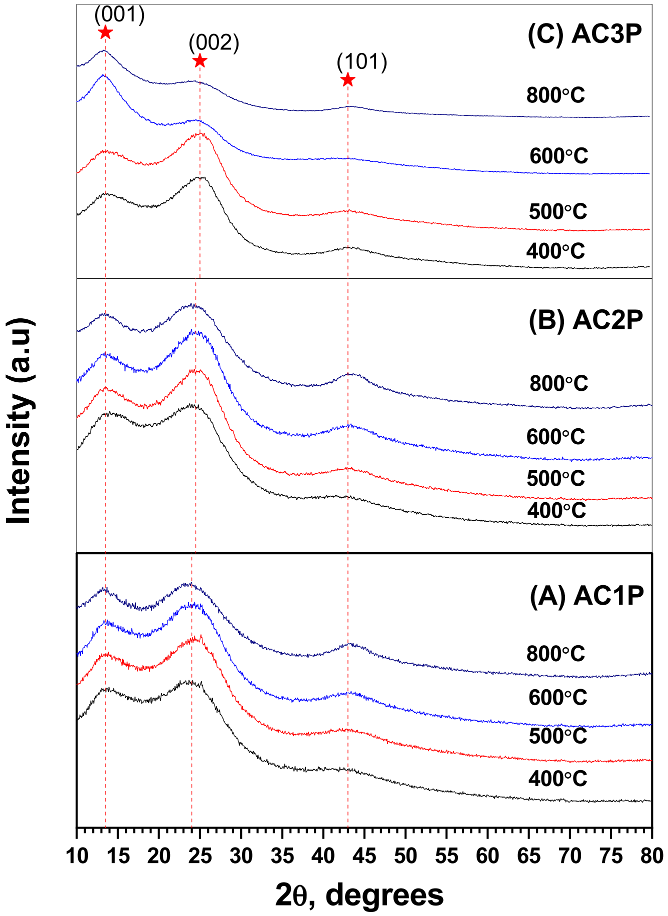

Fig. 1. XRD of the AC1P1, AC2P and AC3P groups of materials at different activation temperatures as indicated.

range of 2–3 nm. These results indicates the formation of small nano-sized amorphous graphite particles <3 nm, where each particle composed of a few graphene layers.

The distance between graphene layers along the *c* axis was estimated by applying the Bragg's equation ($n\lambda = 2d_{hkl} \sin\theta$), to the (002) reflection planes at 24.2°. Thus, an average values of $d_{002} = 0.365$ nm was obtained. Similar procedure was performed to the distance between (001) reflection planes of graphene oxide at 13.13° for estimating the distance between planes. Thus, a value of $d_{001} = 0.650$ nm was obtained. The later value of $d_{001} > 2 \times d_{002}$, which can be explained in terms of the increased separation between the graphene layers due to surface oxidation.

3.2.2. Raman spectroscopy

Raman spectroscopy was carried to investigate the structure of the formed carbonaceous materials. Spectra obtained for the AC2P500 and AC2P600 materials, are shown in Fig. 2. Thus, three peaks related to the D peak, G peak and 2D (weak) were observed. The D peak of disordered graphite structure was observed at about 1354 cm^{-1} and 1347 cm^{-1}, for the AC2P500 and AC2P600, respectively. The G peak of sp^2 bonded carbon atoms in hexagonal lattice was observed at about 1601 cm^{-1} and 1610 cm^{-1}, for the AC2P500 and AC2P600, respectively [49]. The intensity ratio of D peak and G peak (I_D/I_G) were 0.90 and 0.92 for the AC2P500 and AC2P600 materials, respectively. These ratios indicate graphene formation, which increases with increasing of activation temperature. At the same time, very weak degree of graphitization (ordered stacking of graphene layers) were observed for AC2P500 and AC2P600 materials as can be reflected from the intensity of the 2D peak at 2680 cm^{-1}, which is highly sensitive to stacking of graphene sheets [50,51]. Thus, Raman spectra suggested that the nanosized particles (detected by XRD results above) are composed of distorted graphite structure with low stacking of graphene layers. That is the nanoparticles are composed of few graghene layers.

3.2.3. ATR-FTIR spectroscopy

FTIR-ATR spectroscopy of the AC1P and AC3P group of adsorbent materials, which were activated at different temperatures, are shown in Fig. 3. The spectra were matched with the reported vibrational group frequencies characteristic for activated carbon and/or P-doped carbonaceous materials [52,53]. Thus, the observed bands were categorized in two groups; the first was related to C, H, and O bonding, whereas the second was related to C, O and P bonding.

For the first group of bands, the weak intensity band around 2960 cm^{-1}, was assigned to asymmetric ν(C–H) in –CH_3 groups; and the weak bands at 2920 and 2850 cm^{-1} were assigned to asymmetric/symmetric ν(C–H) in –CH_2– groups. These different (C–H) bands were disappeared with increasing of the activation temperature (≥600 °C), which indicates increasing of aromatization with increasing of the activation temperature. The band at 1690 cm^{-1} was assigned to (C=O) absorption of carboxylic groups. The intensity of the later (C=O) band assigned for carboxylic groups was decreased by increasing of the activation temperature from 400 to 500 °C and completely disappeared at higher activation temperatures. The band observed at 1570 cm^{-1} was assigned to ν (C=C) of aromatic rings, which indicates the presence of single or multiple aromatic rings in the carbon skeleton [54]. The aromatic character was further confirmed by the bands at 880, 820 and 760 cm^{-1}, which were related to δ (C–H), aromatic out-of-plane bending vibrations. The band at 486 was assigned to δ (C–O) and δ (C–C) symmetric bending vibrations. The band at 1430 cm^{-1} was assigned to δ (O–H) bending of phenol type surface groups. The band observed at around 1150 cm^{-1} was assigned to oxidized carbons and also assigned to ν (C–O) stretching in acids, alcohols, phenols, ethers and esters.

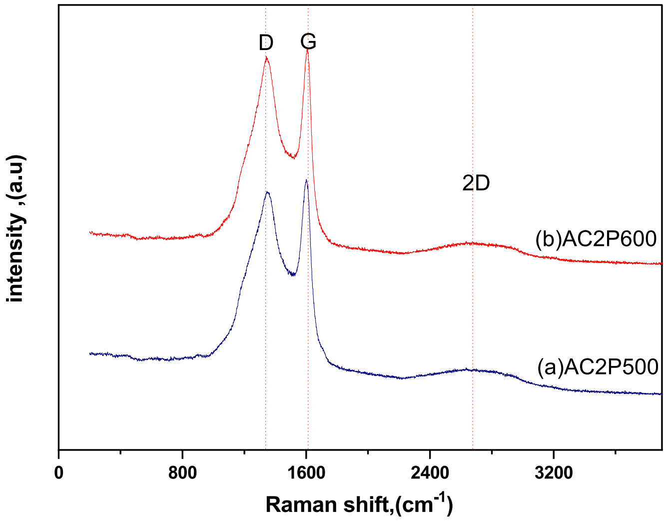

Fig. 2. Raman spectroscopy of AC2P500 and AC2P600.

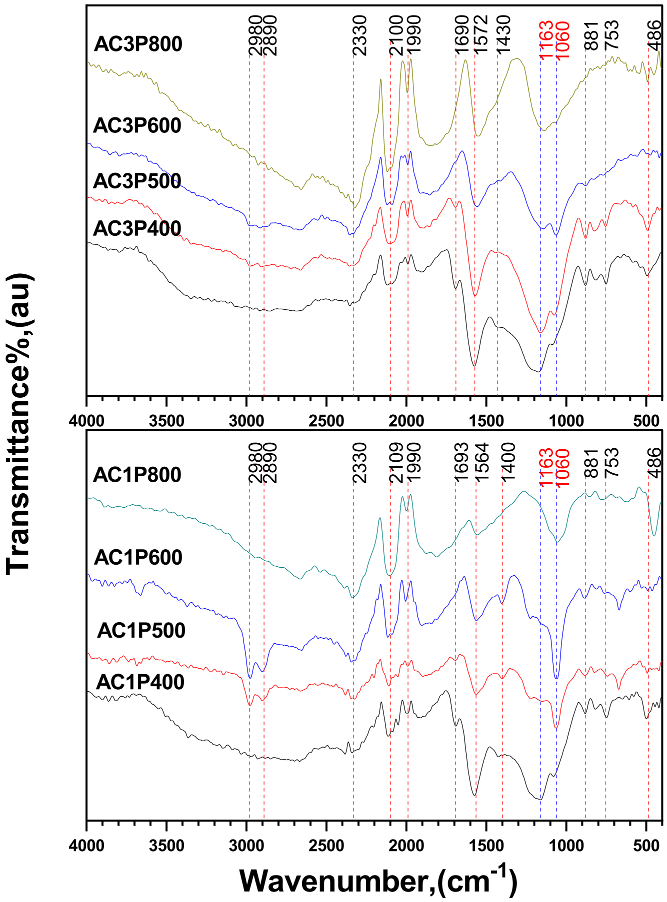

Fig. 3. ATR-FTIR of AC1P and AC3P groups of materials activated at different temperatures as indicated.

For the second group of bands, which were related to the C, O and P bonding, the band at 1163 was assigned to the stretching vibration of hydrogen-bonded P–O groups from phosphates or polyphosphates, and also to the O–C stretching vibration in the P–O–C (aromatic) linkage and to O=P–OH. The band at 1060 cm^{-1} is attributed to the P–O–C bonds of acidic phosphate esters, in addition to the symmetric vibrations in the P–O–P chain [55].

The above FTIR−ATR spectra, Fig. 3, showed some more interesting information about the effect of activation temperature on the stability of different functional groups. Specially, the less stable CO_2 releasing groups (e.g. carboxylic, lactone groups) that observed for the ACPs activated at 400 and 500 °C, were completely disappeared for ACPs activated at 600 and 800 °C. Also, most of the more stable CO releasing groups (phenols, anhydride, carbonyl, ether, and quinone) were removed at 800 °C, specially, for the AC3P800 material formed with high H_3PO_4 acid ration. This process is clearly related to the relative stability of groups at high temperatures, which increased with the increasing of acid ratio.

3.2.4. Thermal analysis

Simultaneous (TG–DTA) analyses were carried out for the AC1P500, AC1P600 and AC1P800 materials. The obtained TGA curves along with their first derivative curves DTG curves in the flow of nitrogen gas or air are shown in Fig. 4. The decomposition process occurred in the flow of nitrogen gas can be divided into three steps. The first step RT−400 °C showed a DTG maxima below 100 °C and a stable mass region in the range of 100–400 °C. Weight loss of ~15% was recorded in this step, which associated with loss of moisture and light weight volatiles (CO, CO_2 and some other hydrocarbons), which formed by catalytic degradation of biomass materials with phosphoric acid [56–59]. The second step 400–800 °C, showed a significant weight losses up to ~79%. The DTG peaks observed in the second step were large with double maximum at (575 and 610° C), (589 and 620 °C) and (731 and 776 °C) for AC1P500, AC1P600 and AC1P800, respectively. Thus, the decomposition peak maxima were moved to high temperatures with increasing of the activation temperatures, which indicates increasing of thermal stability in the ordere of AC1P500 < AC1P600 < AC1P800. The observed weight losses and degradation of AC1P materials in this step were originated from the volatilization of phosphorus compounds (including H_3PO_4,$H_2PO_4^-$ and $H_2P_2O_7^{2-}$), which starts to eliminate from cellulose phosphate esters above 400 $^{\circ}$C [44,60]; removal of P_2O_5 above 500 °C [61,62] and carbon loss due to the oxidation of P_2O_5 [63]. The third step (800–1000 °C) showed no significant weight loss for all the test samples in flow of N_2. The results are summarized in Table S2.

The corresponding TGA results in the flow of air for the AC1P500, AC1P600 and AC1P800 are shown in Fig. 4, as indicated. TGA curves for ACP materials in flow of air are largely modified, but the decomposition still occurs in three steps. The DTG peaks were sharpened and shifted to lower temperatures (than curves carried out in flow of N_2) and showed one sharp peak maximum at 530, 560 and 587 °C for AC1P500, AC1P600 and AC1P800, respectively.

The simultaneously measured DTA curves for the AC1P500, AC1P600 and AC1P800 in the flow of nitrogen gas or air are shown in Fig. 5, as indicated. In the flow of nitrogen, the DTA curves showed a strong exothermic peak maximized at 540, 549, and 588 °C for the AC1P500, AC1P600 and AC1P800 materials, respectively. However, in the flow of air the exothermic peaks were sharpened and shifted to lower temperatures at 494, 532, and 578 °C, for AC1P500, AC1P600 and AC1P800, respectively. The DTA results are summarized in Table S2.

3.3. Texture assessment and nanostructure morphology

3.3.1. Nitrogen adsorption isotherms and porosity

Nitrogen adsorption/desorption isotherms of AC1P, AC2P and AC3P groups of materials, which were activated at different temperatures, are shown in Fig. 6. Inspection of the isotherms indicates that there were rapid increases of N_2 adsorption at low relative pressure ($p/p^o < 0.10$). Whereas, clear multilayers adsorption regions were formed at higher relative pressure, $\geq$ 0.4.

The isotherms of AC1P materials activated at different temperatures (400−800 °C), Fig. 6, showed large adsorbed nitrogen volumes and were classified as type IV of isotherms with a hysteresis loops of type H4, which characterizes narrow slit shaped pores. However, the presence of some relatively constant adsorbed volume at high p/p^o indicates the presence of samll size nanoporosity, which was confirmed by the *t*-plot analysis, as shown below.

The isotherms of AC2P and AC3P groups of materials activated at different temperatures (400−800 °C) Fig. 6, showed larger adsorbed volumes, which were increased with increasing of acid ration (AC2P < AC3P) and decreased with increasing of the activation temperature (400 > 500> 600 > 800 °C). The isotherms were classified as type IV of isotherms with hysteresis loops of type H3, which indicates wide slit

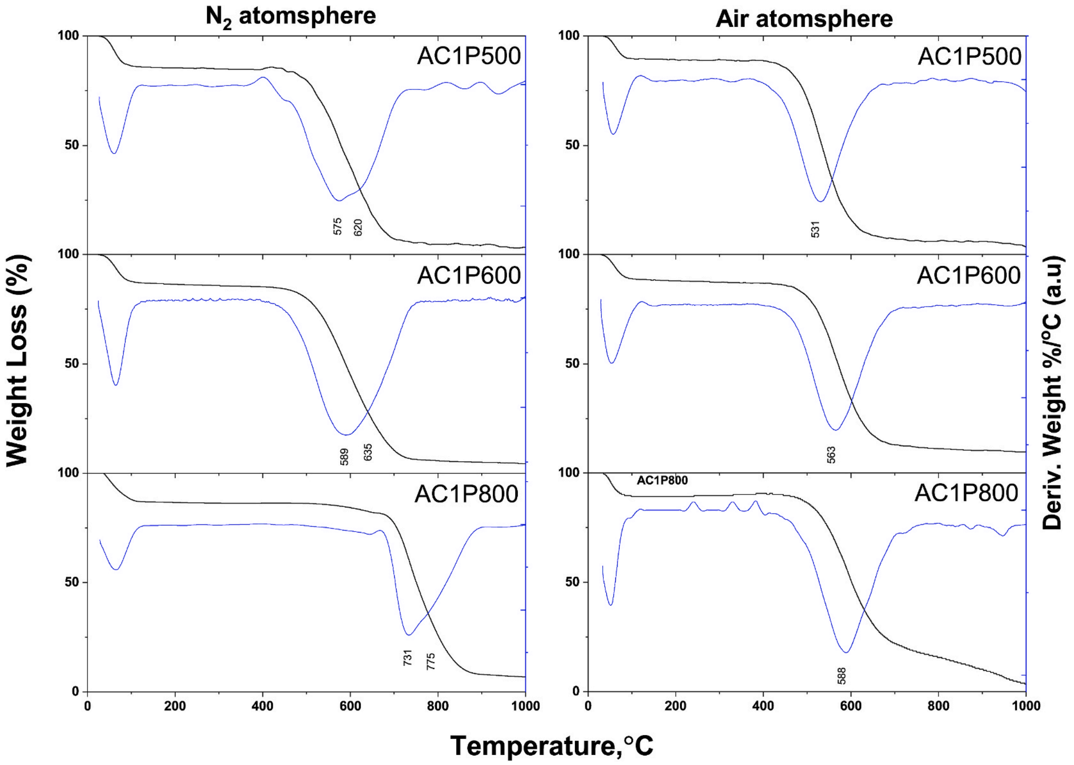

Fig. 4. TGA and DTG curves of AC1P500, AC1P600 and AC1P800, carried out in flow of N_2 or air atmosphere, as indicated.

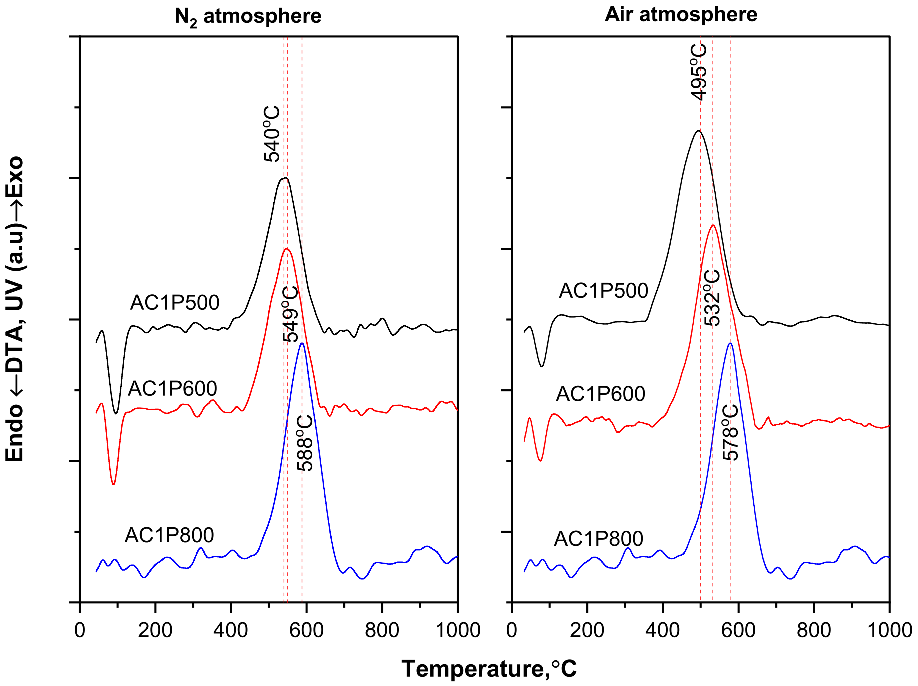

Fig. 5. DTA curves of AC1P500, AC1P600 and AC1P800, carried out in flow of N_2 or air atmosphere, respectively.

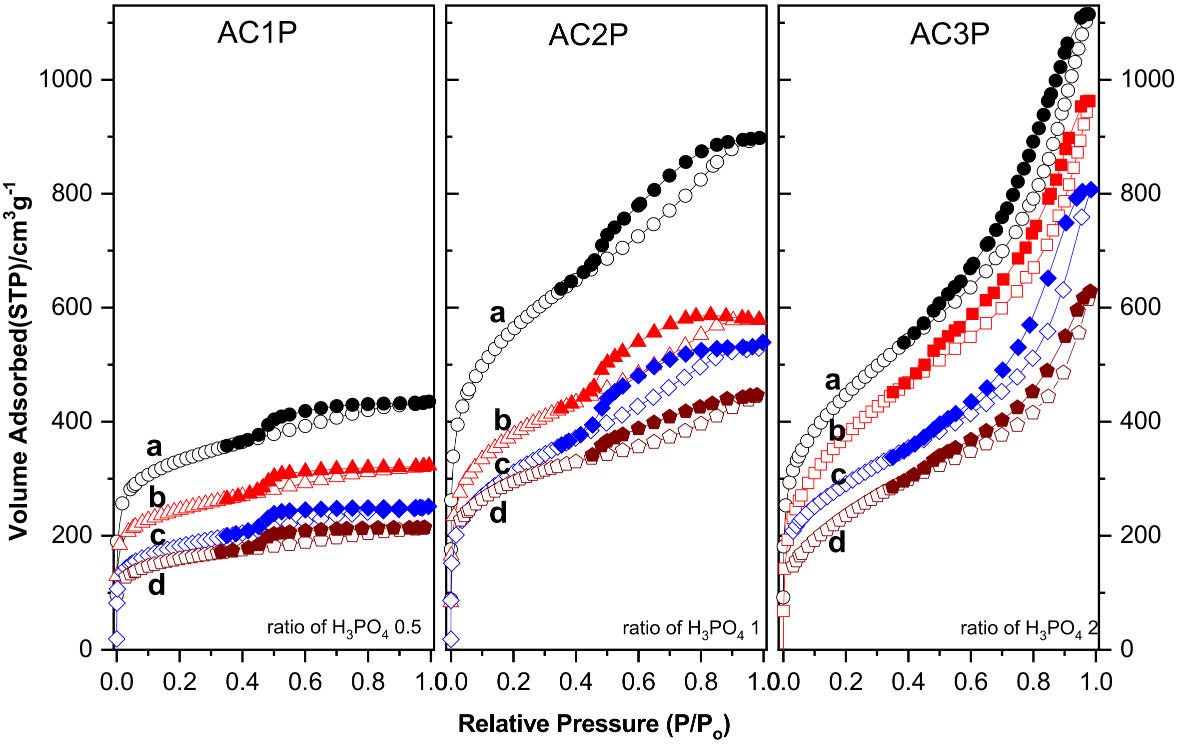

Fig. 6. N_2 adsorption/desorption isotherms obtained with AC1P, AC2P and AC3P groups of materials activated at different activation temperatures as (a) 400, (b) 500, (c) 600 and (d) 800 °C.

shaped porosity. It is known that the type H4 and H3 loops are observed with aggregates of plate−like particles giving rise to narrow and wide slit-shaped pores, respectively. Therefore, increasing of acid ratio and activation temperature can be discussed in terms of widening of the slit shaped pores that formed by the plate-like aggregates of ACP nanoparticles. This discussion is supported by XRD results shown above, and HRTEM as shown below.

High surface area, S_{BET}, values of 1144−580, 1452−1067, and 1706−1204 m^2/g, were obtained for the AC1P, AC2P and AC3P groups of materials, respectively. Generally, the S_{BET} values increased with increasing of the acid ratio (AC1P < AC2P < AC3P) and decreased with increasing of the activation temperature (400 > 500> 600 > 800 °C). The highest S_{BET} value (1706 m^2/g) was obtained for the AC3P400 material. Textural details including S_{BET}, S_t, and S_{mic}, values are cited in

Table 2. The *t*–plot analysis for the ACP materials showed linear fitting for all plots at the initial portion of the *t*−curves that can be interpolated to intercept at the origin point of the plot. These behaviors indicate the presence of small size mesoporosity and/or supper-micro porosity (1.0–2.0 nm).

Further textural details including total pore volume, V_p (estimated at p/p^o of 0.95) and micro pore volume, V_{mic} (estimated at $p/p^o = 0.1$), ($V_{meso} = V_p - V_{mic}$), P_{meso}% ($V_{meso}/(V_{mic} + V_{meso}) \times 100$), pore width, and W_p (by the average $4V_t/S_{BET}$ and BJH methods) were calculated and cited in Table 2. Both of the V_T and V_{meso} values were found to increase with increasing of the acid ratio and decrease with increasing of activation temperature. However, mesoporosity percentages, P_{meso}(%), and W_p, were generally increased with increasing of both of acid ratio and activation temperature. Little, exception was found for AC3P800, which was due to the blocking or reducing of the pore size as a heat shrinking effect [64]. Pore size distributions, PWDs, obtained by the BJH method, for AC1P, AC2P and AC3P group of materials are presented in Fig. 7. Inspection of the PWDs confirms progressive enhancing and widening for pore size distribution with increasing of the acid ratio (AC1P < AC2P < AC3P).

Textural comparison of the formed materials with recently reported materials, reflects that the present ACP materials show higher surface areas as well as higher contribution from mesoporosity (up to 94%), as shown below.

3.3.2. Transmission electron microscopy (SEM), EDX and elemental mapping

Nanostructure morphology at different magnifications was investigated with TEM and HRTEM imaging. The micrographs obtained for the AC3P800 at different successive magnifications are presented in Fig. 8 (A, B, and C), respectively. The HRTEM micrographs confirmed the plate-like nature of the graphite particles. Moreover, Selected Area Electron Diffraction (SAED) pattern, Fig. 8 (D), showed a diffuse type diffraction rings, which indicates that the 3D nanostructure is disordered, i.e. without well ordered graphene layer stacking into graphite–like structure. This result is on line with the Raman spectroscopy results shown above. The micrographs confirm the plate−like particles formation, which were resulting from the interaction of phosphoric acid with the OP material, which subsequent volatilization of gaseous species, leaving behind the observed carbonaceous plate-like material [65].

Moreover, EDX spectra for AC3P800 was obtained and presented as shown in Fig. 9 along with the elemental mapping for the main constituent elements (C), (O), and (P), which were amounting to 85.96, 7.53 and 5.96%, respectively. Some other minor elements (Na, Si and K) were also detected, which were of 0.16, 0.12 and 0.26 mass %, respectively. Elemental mapping for the main constituent elements (C), (O), and (P) in the AC3P800 material showed very homogenous dispersions [36].

3.4. Adsorption of methylene blue, MB

3.4.1. Preliminary investigation

3.4.1.1. Effect of ACP dosage and contact time. The adsorption capacity and removal percentage of MB were investigated at different adsorbent dosages (0.200–8.00 g/L), fixed initial concentration of MB (600 mg/L) and pH of 6.5. Results obtained with the AC3P800 material, indicated that with increasing of the ACP dosage the adsorption capacity and removal percent were increased due to the presence of more carbon surface and more adsorption sites (Fig. S2).

The removal percentage was explored against the effects of (i) increasing of phosphoric acid ratio (at constant activation temperature), and (ii) increasing of activation temperature (at constant acid ratio). Results indicated that the removal percent was amounting to 59, 61, 80 and 96 for AC3P activated at 400, 500, 600 and 800 °C respectively. Whereas, the removal percent was amounting to 55, 66 and 96 for AC1P, AC2P and AC3P activated at 800, respectively. Thus, the adsorption capacity and removal percentage were increased with increasing of phosphoric acid ratio and with increasing of activation temperature (Fig. S3). Therefore, the AC3P800 material was the most active adsorbent towards MB.

3.4.1.2. Point of zero charge and effect of pH. The pH value at the point of zero charge, pH_{PZC}, was evaluated from the graphical plot of ΔpH against the initial pH values, as shown in Fig. 10 (A). The determined pH_{PZC} was of 6.3, which indicates that the adsorbent surface is positively charged for $pH < pH_{PZC}$, and the adsorption of cationic dye was lowered. Whereas, the adsorbent surface is negatively charged for $pH > pH_{PZC}$, and the adsorption of cationic dye was enhanced.

The effect of pH on the q_{ads} and the removal percentage of MB are shown in Fig. 10 (B). The adsorption capacity was lowered at lower pH values, due to the presence of more H^+ in acidic solution that compete with the active adsorbent sites towards the MB molecules. However, significant increase in adsorption capacity was observed at neutral and alkaline pH conditions. This was because more negative charge were created on the adsorbent surface, which led to adsorption of more MB cationic species by electrostatic attraction [66].

3.4.1.3. Desorption and regeneration studies. Different eluents were

Table 2

Surface Texture characteristics of the OP_derived ACP materials (specific surface area (S_{BET}), external surface area (S_{Ext}), micropore area (S_{mic}), total adsorbed volume (V_T), micropore volume (V_{mic}), mesopore volume (V_{meso}), mesoporosity percentage (P_{meso} %) and pore diameter (P_D).

Sample	S_{BET} (m²/g	S_{Ext} (m²/g)	S_{micro} (m²/g)	V_T (ccm/g)	V_{micro} (ccm/g	V_{meso} (ccm/g)	PMeso (%)	PW(BET) (A°)	PW(BJH) (A°)
AC1P400	1144	492	652	0.635	0.272	0.364	57.2	22.2	35.4
AC2P400	1452	970	482	0.984	0.200	0.784	80	27.01	41.2
AC3P400	1706	1394	283	1.536	0.123	1.419	92.3	36	50.2
AC1P500	983	426.3	557	0.553	0.233	0.320	58	23.1	34.4
AC2P500	1356	894	462	0.894	0.191	0.703	79	26.6	38.3
AC3P500	1600	1324	276	1.630	0.111	1.520	93.2	41.4	54.2
AC1P600	855	343	512	0.460	0.189	0.271	59	23.3	32.9
AC2P600	1265	865	400	0.892	0.179	0.714	80	28.2	38.9
AC3P600	1522	1212	310	1.713	0.111	1.602	94	42.3	57.3
AC1P800	580	277	303	0.328	0.129	0.199	61	22.6	34
AC2P800	1067	724	346	0.6782	0.1809	0.4973	73	25.4	37
AC3P800	1204	923	281	1.0145	0.1112	0.9033	89	34	50

V_T calculated at at (p/po = 0.95).
V_{mic} calculated at (p/po = 0.10).

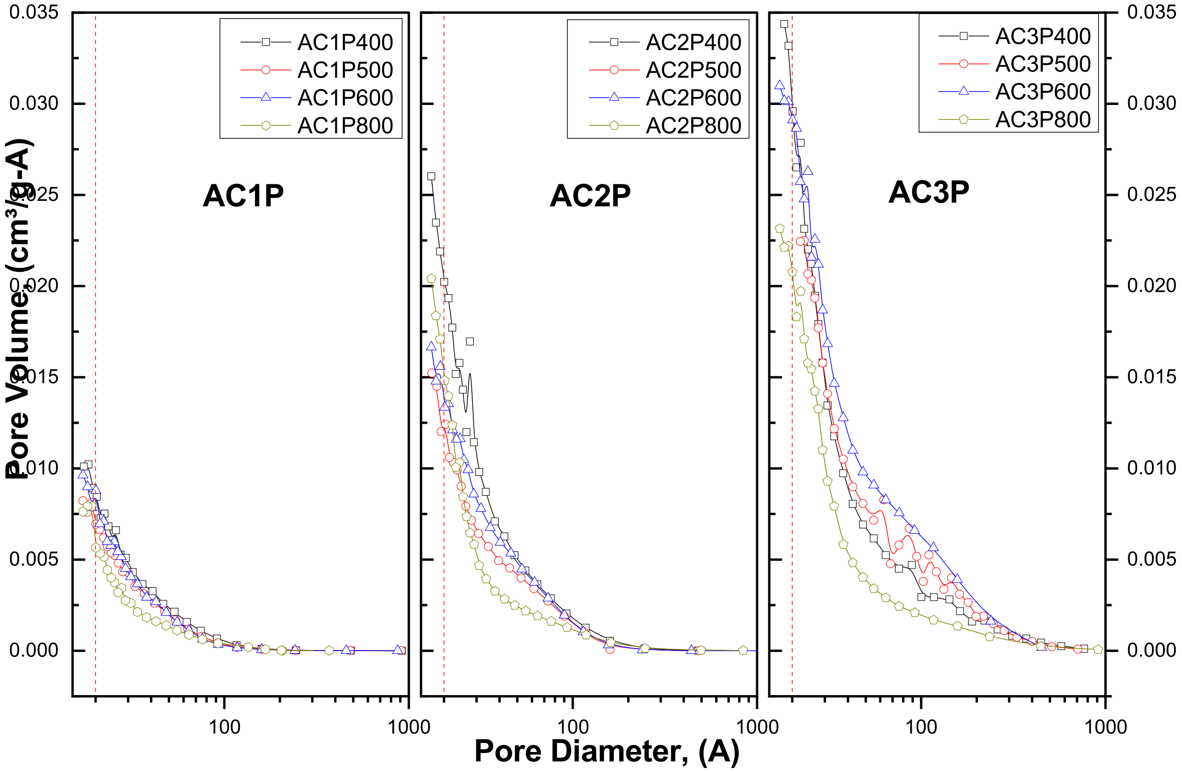

Fig. 7. Pore size distributions (BJH method) obtained from the adsorption branches of N_2 adsorption/desorption isotherms obtained with AC1P, AC2P and AC3P groups of materials.

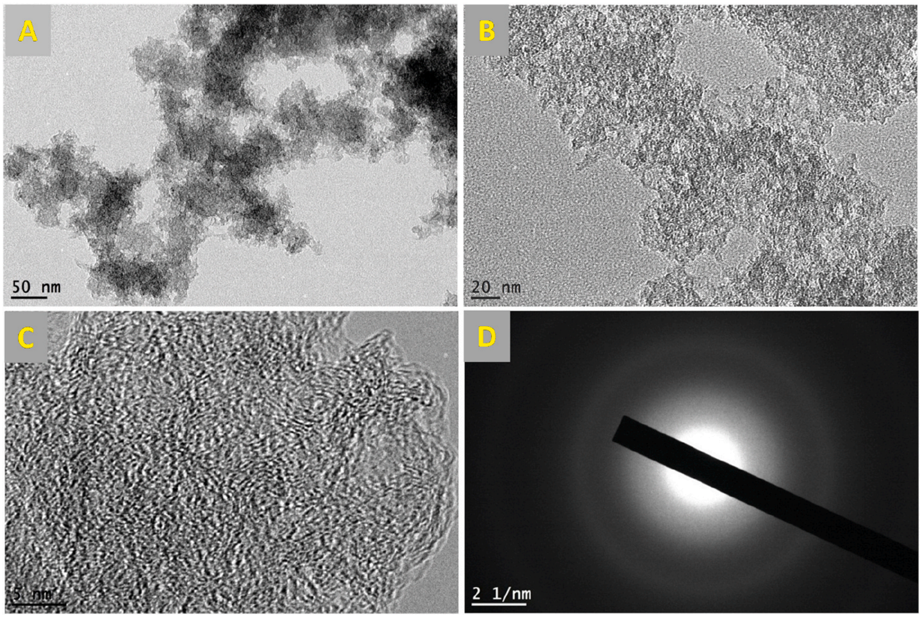

Fig. 8. HRTEM micrograph for the AC3P800 material at successive magnifications (a), (b) and (c) as indicated by the inserted scale bars (50, 20 and 5 nm, respectively), along with a typical small area electron diffraction, SAED (d).

examines (absolute ethanol, HCl (1 *M*), ethanol−HCl (9:1) mixture, HNO_3 (1 *M*) and NaOH (1 *M*) solutions) for desorption of MB from the spent adsorbent. Results showed that the desorption efficiency of MB were 88.6, 73, 42, 18 and 3.2%, for the ethanol−HCl mixture, absolute ethanol, HCl, HNO_3 and NaOH solutions, respectively (Fig. S4). Thus, the best eluent was employed.

Desorption of the adsorbed MB molecules and reusability of the adsorbent materials for successive cycles was investigated, Fig. 10 (C). It was found that reasonable MB adsorption percentages (96.89, 93.58, 87.17 and 76.82%) and desorption percentages (of 88.61, 79.92, 71.85 and 65.99%) were obtained for the first, second, third and fourth cycles, respectively. This result reflected that the adsorbent exhibited good regeneration and reusability characteristics.

3.4.2. Adsorption isotherms of MB

Empirical adsorption isotherms of MB on the AC1P, AC2P and AC3P

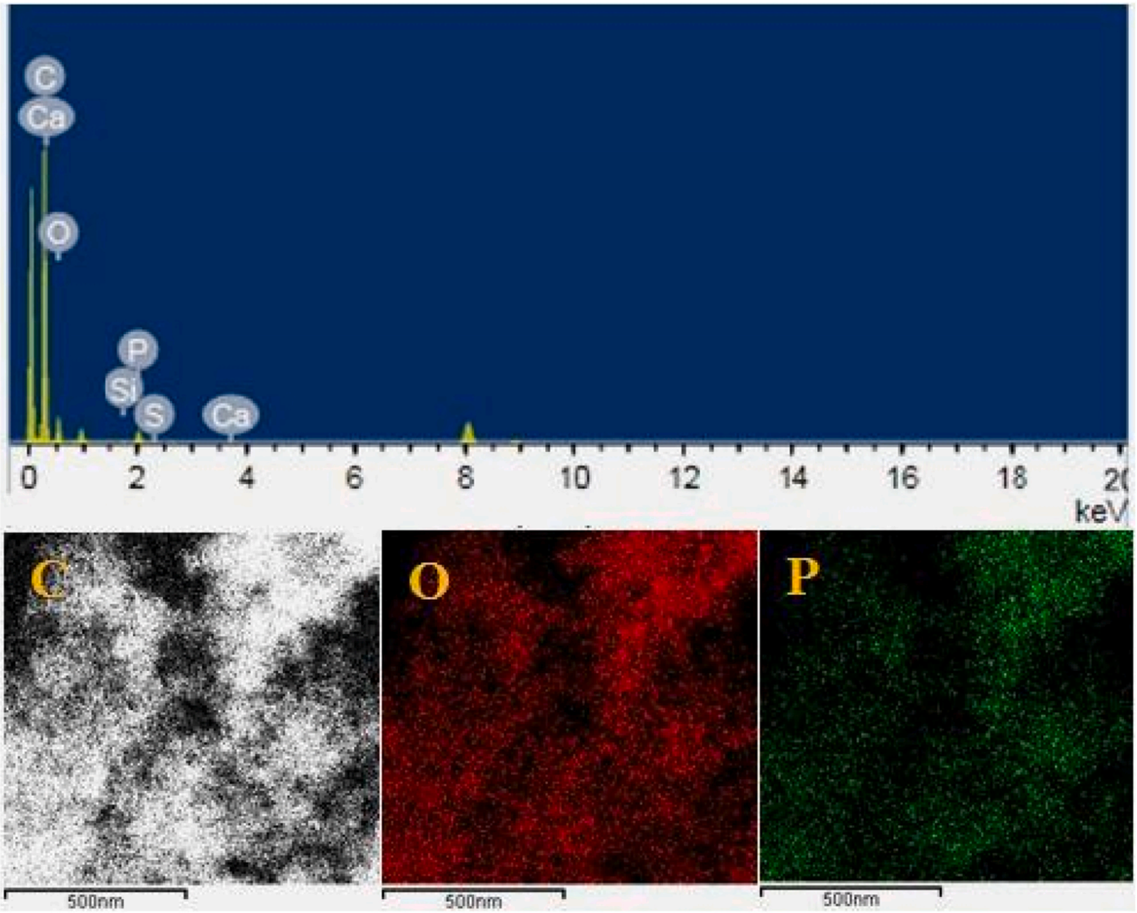

Fig. 9. TEM-EDX elemental analysis of the AC3P800 material along with elemental mapping for C, O, and P elements as indicated.

adsorbent groups are shown in Fig. 11 (A, B and C), respectively. Inspection of the isotherms showed that the (q_{ads}) values were increased with increasing of the acid impregnation ratio (AC1P $<$ AC2P $<$ AC3P) and with increasing of the activation temperature within each group ($400 < 500 < 600 < 800$ °C). Results showed that high adsorption capacity, q_{ads}, as high as 452 mg/g were obtained for the most active sample (AC3P800) at equilibrium concentration, C_{eq}, of 300 mg/g.

More information can be gained by inspection of the empirical adsorption isotherms in light of Giles classification [67,68] for adsorption from solutions. Accordingly, the examined materials can be classified into two categories. The first category, which includes all the isotherms obtained with adsorbents formed at low acid ratios and low activation temperature, were classified as type L (Langmuir class) of subclass (L4). Whereas, the second category, which includes all the isotherms obtained with adsorbents formed at high acid ratios and high activation temperature, were classified as type L (Langmuir class) of subclass (L2). Thus, the classification characterizes multilayer and monolayer adsorption of cationic MB species for the first and the second categories, respectively. The departure of the subclass from L4 to L2 emphasized that number of adsorption sites was increased with increasing of acid ratios and activation temperature.

To characterize the nature of the adsorption process, the adsorption isotherms were examined with a group of potential adsorption isotherm models, which are frequently employed for similar adsorption processes. Namely, the Langmuir [69], Freundlich [70], Tempkin [71], Dubinin-Radushkevich [72] isotherm models. The nonlinear and linear equation forms as well as the parameters describing these isotherm models are cited in Table 3.

The numerical values obtained by application of the above indicated isotherm models for the AC1P, AC2P and AC3P group of adsorbents were calculated (Table S3 (A, B, and C), respectively). Accordingly, the Langmuir model fits gave rise to r^2 values close to unity (r^2 = 0.9999–0.8952). Wheareas, lower values were obtained for Temkin (r^2 = 0.9664–0.6396), Dubinin−Radushevish (r^2 = 0.9564–0.4143) and Freundlish (r^2 = 0.9761–0.5172) isotehrms. Therefore, the applicability of the examined isotherms models for the present adsorption process was in the order of: Langmuir > Temkin > Dubinin- Radushevish > Freundlich isotherm model (Fig. S5).

The applicability of Langmuir isotherm model implies energetically homogeneous surface for the ACP materials and monolayer coverage of the MB dye molecule. This situation was met for the ACP adsorbent materials, specially, for those obtained at higher activation temperatures.

In terms of the applicability of Langmuir isotherm model, the favorability of the adsorption process was examined. The values of the dimensionless separation factor (R_L) were calculated for the ACP adsorbents, Table S3 (A, B and C). The values of the separation factor was found to be 0.001 (i.e. $0 > R_L < 1$), which confirms favorable nature of the adsorption process.

Therefore, statistical analysis of the different models for the most active sample (AC3P800), Table 3, confirmed that the best fit was obtained with the Langmuir model. Therefore, the nonlinear Langmuir model fitting was generated for the most active sample are shown (along with the experimental data) in Fig. 12.

Furthermore, statistical assessment of the fitting accuracy of with each model was tested by a group of statistical parameters. Thus, the R^2 (coefficient of determination), *RMSE* (root-mean-square error, and ARE (absolute relative error) were calculated according to the following Eq. (9−11), respectively.

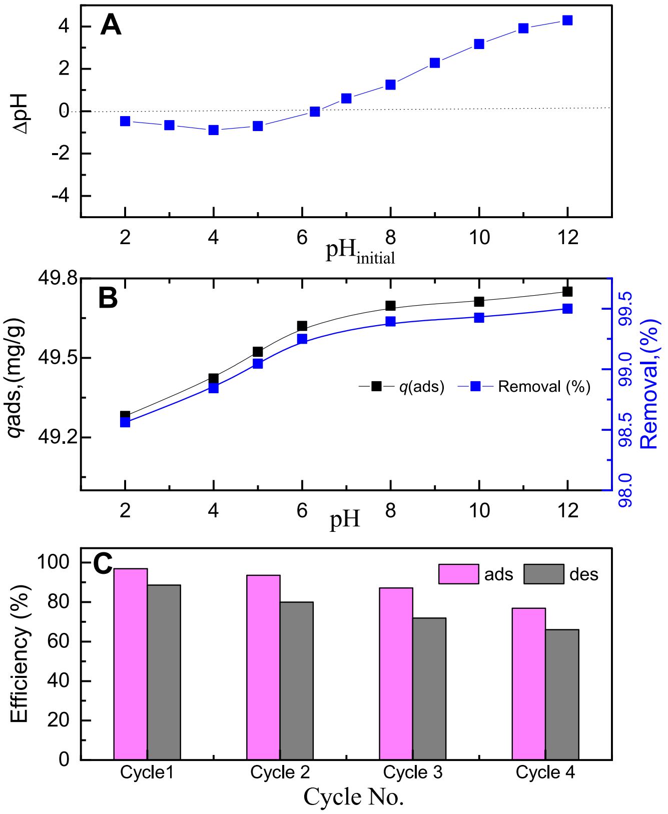

Fig. 10. Point of zero charge (A), effect of pH on the amount adsorbed and removal percentage (B), and efficiency of recovery against number of cycle (C) for the most active sample AC3P800.

$$R^2 = 1 - \frac{\sum_{i=1}^{n}\left(q_{e,exp} - q_{e,cal}\right)^2}{\sum_{i=1}^{n}\left(q_{e,exp}\right)^2 - \left[\left(\sum_{i=1}^{n} q_{e,exp}\right)^2 \Big/ n\right]} \tag{9}$$

$$\mathrm{RSME} = \sqrt{\frac{1}{n}\sum_{i=1}^{n}\left(q_{max} - q_{cal}\right)^2}$$

$$\mathrm{ARE} = \frac{100}{n}\sum_{i=1}^{n}\left|\frac{q_{i,model-q_{exp}}}{qexp}\right| \tag{11}$$

The statistical parameters R^2, *RSME* and *ARE* values obtained from nonlinear fits are listed in Table 4. Analysis of these parameters allows more information about the nature of the adsorption process and the surface properties of the adsorbent [73–75]. Thus, the best non-linear fit was obtained with the Langmuir adsorption model as the highest R^2 (0.93817) beside lowest value for *RSME* (23.15) and *ARE* (11.98were obtained. This in fact confirms the above predicted applicability of the Langmuir isotherm model.

3.4.3. Kinetics of MB adsorption

The adsorption kinetic studies were carried out to evaluate the ACP adsorbent materials on MB adsorption against time in order to obtain more information the adsorption processes.

Results for AC3P800 adsorbent material at different MB initial concentrations (50–800 mg/L) were investigated. The rate of reaction was investigated with the pseudo-first-order, pseudo-second-order, and intra−particle kinetic models to find out the suitable kinetic model to explain the mechanism of adsorption process. The linear forms expressions Eqs. (12)–(14); as well as the non-linear expressions Eqs. (14)–(16) for the pseudo-first-order, pseudo-second-order, and intra−particle models, respectively, are represented below.

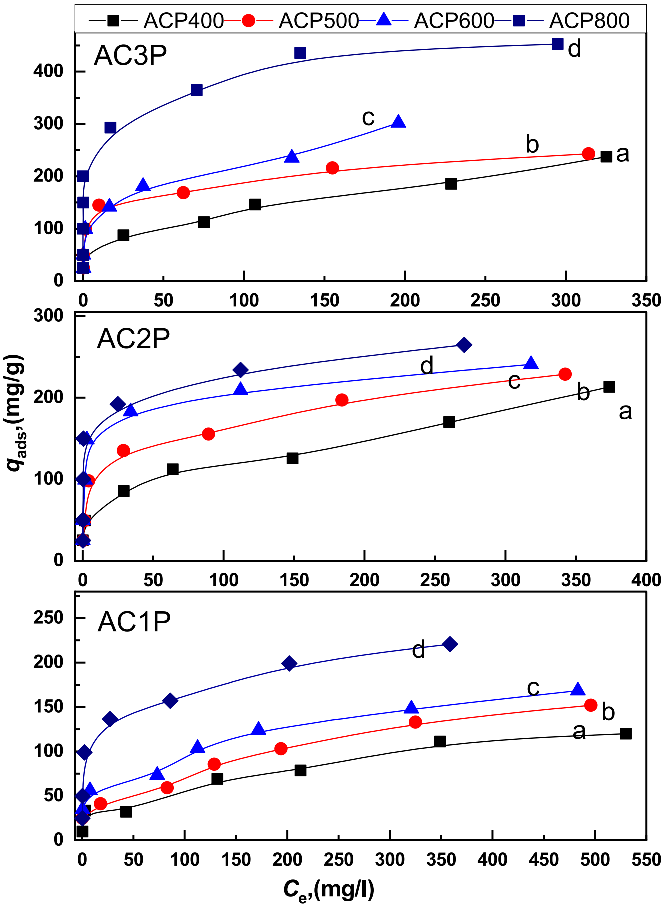

Fig. 11. Adsorption isotherm of MB from solutions obtained with AC1P, AC2P and AC3P materials activated at different activation temperatures as (a) 400, (b) 500, (c) 600 and (d) 800 °C.

Table 3
The examined adsorption model names, equations (nonlinear and linear) form, and their parameters.

Models	Equation	Parameters
Langmuir isotherm [69].	$q_e = \frac{q_{max-K_lC_e}}{1+K_{lC_e}}$ $\frac{C_e}{q_e} = \frac{1}{q_{max}K_L} + \frac{1}{q_{max}}C_e$	C_e = the equilibrium concentration (mg/*l*), q_e = the equilibrium adsorption capacity (mg/g), q_{max} = the maximum adsorption capacity (mg/g), and K_L is the Langmuir constant (*l*/mg). R_L = the separation factor = 1/(1+K_LC_0)
Freundlich isotherm	$q_e = k_f c_e^{\frac{1}{n}}$ $logq_e = logK_F + (1/n)logC_e$	K_F = Freundlich adsorption constant (mg/g) $(mg/l)^{1/n}$ 1/n = the adsorption intensity parameter (1/n), with a value b
Dubinin-Radushkevich (D-R) [72].	$q_e = q_s e^{(-\beta_{DR}\cdot\varepsilon^2)}$ $\varepsilon = RT\ln\left(1 + \frac{1}{C_e}\right)$ $\ln q_e = \ln q_s - \beta\epsilon 2$	q_s = the theoretical monolayer saturation capacity (mg/g), β = the D-K model constant (mol^2 kJ^{-2}), ϵ = the Polanyi adsorption potential, $\epsilon = RT\ln(1 + 1/C_e)$, E = the mean free energy of sorption (kJ/mol) $E = E = 1/\frac{1}{\sqrt{2\beta}}$.
Temkin and Pyzhev isotherm [71].	$q_e = B\ln AC_e$ $q_e = B\ln K_T + B\ln C_e$	B = RT/b_T is related to the heat of adsorption (J/mol), where 1/b_T indicates the adsorption potential of the adsorbent, and K_T = the isotherm constant, dimensionless.

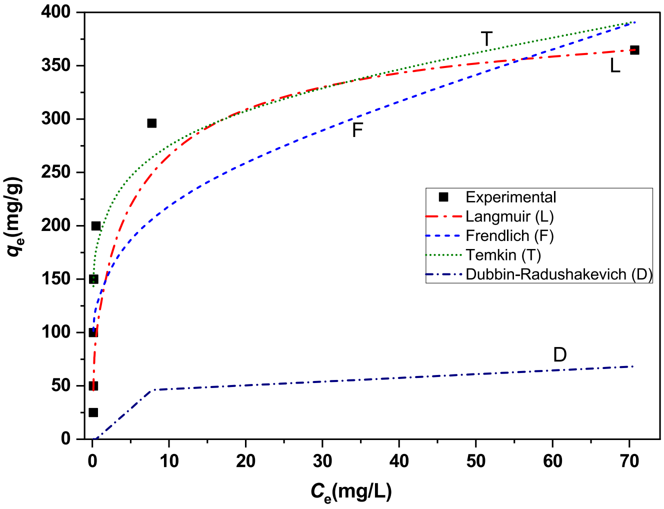

Fig. 12. The nonlinear fits for the Langmuir, Freundlich, Temkin isotherms and Dubbin-Radushakevich of MB adsorption on AC3P800.

Table 4
The statistical analysis parameters for non–linear fits obtained with the indicated adsorption isotherm models for MB adsorption on the most active sample, AC3P800 adsorbent.

Nonlinear Isotherm type	Parameters
Langmuir isotherm	q_{max} (mg//g) = 370 K_l (mg/l) = 1 $R^2 = 0.93817$ RSME = 23.15 ARE = 11.98
Freundlich isotherm	K_f (mg/g)(l/mg)$^{1/n}$ = 155.06 n = 0.2169 $R^2 = 0.8665$ RSME = 51.6 ARE = 43.84
Dubinin–Radushkevich isotherm	q_s (mg//g) = 352.5 β (mg/l) = 0.02312 $R^2 = 0.44374$ RSME = 179.6 ARE = 95.10
Temkin isotherm	$A = 257.23$ B = 39.89 $R^2 = 0.51209$ RSME = 50.27 ARE = 66.86

$$\ln(q_{e-}q_t) = \ln q_{e\,-}\ K_1 t \tag{12}$$

$$\frac{t}{q_t} = \frac{1}{K^2 q_e^2} + \frac{1}{q_e}.t \tag{13}$$

$$q_t = K_{int} t^{1/2} + C \tag{14}$$

$$q_{t=} q_e\left(1 - e^{-K_l t}\right) \tag{15}$$

$$q_t = \frac{q_e^2.K_2.t}{1 + q_e.K_2.t} \tag{16}$$

Where, q_e and q_t are the amounts of MB adsorbed (mg/g) at time t (min), at equilibrium. The rate constants k_1 (h^{-1}) and k_2 (g/mg h) are for pseudo-first order and pseudo-second-order kinetic models, respectively. Whereas, k_int and c are the intra–particle diffusion constants.

The validity of the examined models was first checked from the corresponding linear plots. The values of rate constants (k_1, k_2 and k_int) and regression coefficient (r^2) obtained for the different kinetic models were obtained (Table S4 (A)). It was found that the pseudo-second order kinetic model ($r^2 \geq 0.9999$) represents the adsorption of MB better than the pseudo-first order and intera–particlemodels. The successful fits obtained with the linear pseudo-second order kinetics are shown in Fig. 13 (A)

Nonlinear fits of the above models were generated and the fits parameters obtained at several initial dye concentrations are listed (Table S4 (B). The statistical fits accuracy was tested using error analysis R^2, RSME and ARE. Thus, the nonlinear plots for the pseudo-second order model presents highest R^2 (0.999–0.983) and lowest RMSE (0.040–29.16) and ARE (0.15–6.57) values (Table S4 (B)). The successful fits obtained with the nonlinear pseudo-second order kinetics along with the empirical results are shown in Fig. 13 (B)

This confirms that pseudo–second order model is the most suitable model to describe the empirical adsorption behavior. Moreover, the inapplicability of the intra–particle diffusion plots confirms non-prevailing intra–particle diffusion, i.e. the system approaches equilibrium together with the saturation of adsorption sites.

3.4.4. *Effect of temperature on MB adsorption*

The effect of temperature on the adsorption processes of MB on the adsorbent material was investigated at different temperature (on the range of 298–318 K), at different initial concentrations of MB (200, 300 and 400 mg/L). Plotting of the results obtained with AC3P800 adsorbent at different initial concentrations reflected that the removal (%) was decreased with increasing of temperature, which confirms the

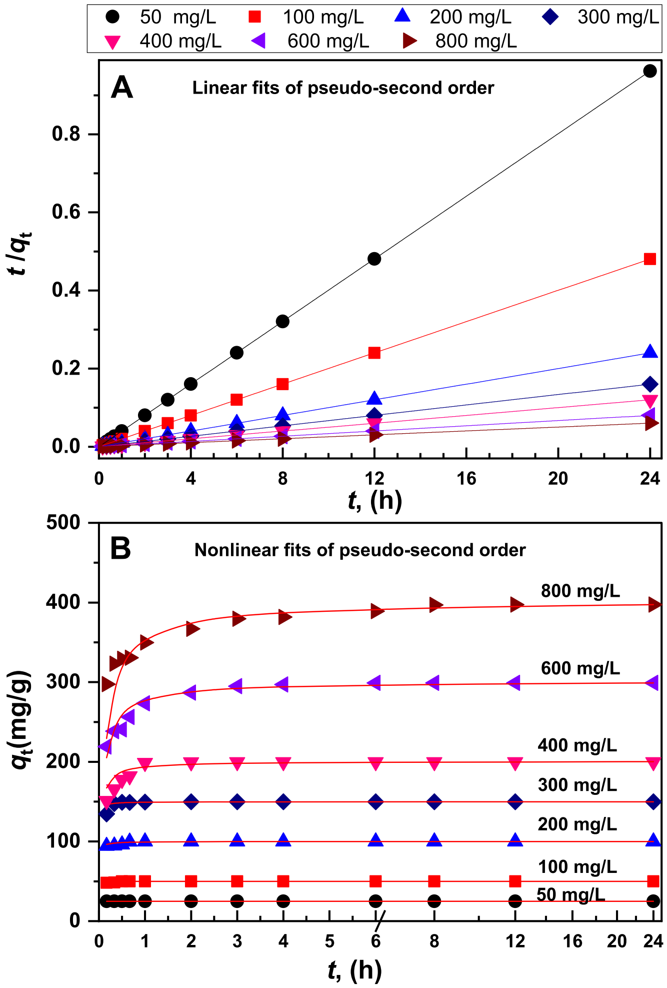

Fig. 13. (A and B): The Linear (A) and nonlinear (B) fits for pseudo-second order adsorption of MB at different initial concentrations (50-800 mg/L, as indicated) on the AC3P800 adsorbent. The symbols represent experimental values and lines represent the fits..

adsorption nature of the present surface process. Thus, the plots of $\ln K_c$ against $1/T$ (the Van't Hoff plots), were obtained for the MB adsorption process on AC3P800, (Fig. S6(A)). The main thermodynamic parameters were calculated using of Eqs. (4) and (5), as standard Gibbs free energy change (ΔG°), −(13.27–14.27); standard enthalpy change (ΔH°), −(12.19–8.78); and standard entropy change (ΔS°), +(0.00362–0.017 kJ/mol). The obtained results confirmed that adsorption of MB on AC3P800 was a favorable process and spontaneous in nature (Table S5). The negative value of (ΔH°) confirmed that the adsorption process was exothermic. The observed small value of ΔS° (<0.017 kJ/mol) however, confirmed good affinity for adsorption of MB on AC3P800. The observed positive sign of randomness in the system for higher concentration was due to replacement of some of the small molecules from the surface of adsorbent due to the presence of large crowd of adsorbate molecules at the adsorbent surface. However, the small values of ΔH°, ΔS° indicated that weak interaction between adsorbent and adsorbate was occurred, which confirms a phyisorption nature of interaction [76,77].

The values of activation energy (E_a) and sticking probability (S^*) were estimated using a modified Arrhenius type equation given in Eq. (7), which related to surface coverage (θ) [78]. The parameter (S^*) is a measure for the potential of an adsorbate to remain on the adsorbent. The (S^*) values correspond to the adsorbate–adsorbent system were obtained (1.93, 8.09 and 15.73 × 10^{-3} kJ/mol) with different concentrations (200, 300 and 400 mg/L), respectively. The values were in the range $0 < S^* < 1$ and are dependent on the temperature of the system. The surface coverage (θ) can be calculated as given by Eq. (6). The linear fits of ln(1-θ) against $1/T$ was plotted, Fig. S6 (B), and the results were listed, Table S5.

Activation energy (E_a) values amounting to (13.40, 10.16, 8.78 kJ/mol) were obtained with concentrations (200, 300 and 400 mg/L), respectively. The obtained low values of E_a (<13.40–8.78 kJ/mol) are in agreement with the magnitude of the calculated ΔG° values [79], and further confirms the physisorption nature of the present adsorption process.

3.4.5. FTIR-ATR of the MB adsorbate on the adsorbent

The FTIR–ATR spectra of the adsorbate MB molecules, MB(*ads*), with the spent adsorbent can give some information about the presence of active functional group and their interaction with the adsorbate molecules during the adsorption process. Thus, FTIR-ATR spectra for the AC3P800 adsorbent before and after MB adsorption are shown in Fig. 14. Typical group of bands related to ACP materials were observed in both cases, however, some new bands were appeared, while some other were disappeared due to the interaction with adsorbed MB molecules, MB(*ads*). Thus, new bands were appeared at 1578 and 1445 cm^{-1}, which attributed to the asymmetric and symmetrical axial deformation of the carboxylate anion [80]. The latter band is also characteristic for heterocyclic stretching vibration of ν (C=N) in MB and (C=C) [81]. The new bands at 2970 and 2890 cm^{-1} are corresponding to the stretching vibrations of aliphatic ν (C–H). The new set of bands appear at 1083, 1228 and 1383 cm^{-1}, are related to aromatic nitro compound and ν (S=O) stretching vibration. Similar bands have been attributed to the existence of MB molecules on the surface of AC materials [82]. On the other hand, the bands in the region from 1800 to 2660 cm^{-1} were completely disappeared after adsorption of MB. These data emphasized the mutual nature of the interaction between MB(*ads*) and the AC3P800 adsorbent material.

3.4.6. Mechanism of MB adsorption on the adsorbent

The mechanism for MB removal from solutions by adsorbent materials can be divided into the following steps [83–85].

1. Migration of MB from the solution bulk to the adsorbent surface.
2. Diffusion of MB through the boundary layer to the adsorbent surface.
3. Adsorption of MB at the active sites of the adsorbent.
4. Intra-particle diffusion of MB into the interior pores of the adsorbent.

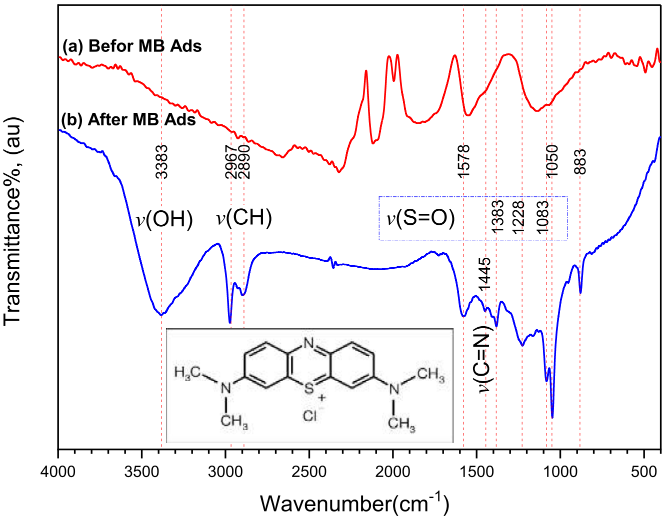

Fig. 14. FTIR–ATR for AC3P800 adsorbent before and after adsorption of MB from solution.

For the present investigation steps number (2) and (4) can be rolled out, respectively because the boundary layer resistance normally reduced by increase in contact time; and the intra-particle pore diffusion model was confirmed non-prevailing as the system approaches equilibrium together with the saturation of adsorption sites. This in fact highlights the advantage of the formed slit-shaped pores of wide opining on the adsorption process by the ACP adsorbents, which were widening at high activation temperatures by the effect of surface oxidation and formation of graphene oxide as reflected by XRD.

Moreover, since the uptake of MB at the adsorbent active sites of ACP is a rapid process. The adsorption rate is due to be controlled by the rate of MB species transfer in liquid phase.

Thus, the mutual affinity of MB species and the adsorption active sites of ACP adsorbents can be attributed to the following interaction forces:

I. electrostatic interaction between anionic oxygenated carbon groups and MB cationic site

This interaction occurred between surface oxygenated groups of the ACP adsorbent and MB cationic (N^+) site in the conjugated MB dye structure. This interaction was supposed to take place for the adsorbent obtained at low acid ratios and low activation temperature (400–500 °C) where the low thermally stable groups (carboxylic and lactone) are present as well as the highly thermally stable groups (phenols, anhydride, carbonyl and ether). However, for the adsorbent obtained at high activation temperatures (600–800 °C), the low thermally stable bulky groups were removed. Thereby, facilitating diffusion of MB species to the adsorbent slit–shaped pores.

II. Electrostatic interaction between anionic phosphate groups and MB cationic site

This type of interaction occurred between different phosphate group (e.g. $\equiv$PO, $=\text{PO}_2$ and $-\text{PO}_3$) and cationic (N^+) sites in the conjugated MB dye structure. This interaction was supposed to take place for the adsorbent obtained at high acid ratio and high activation temperatures, which associated with the formation of acidic phosphate groups.

III. Hydrogen bonding

This type occurred between surface hydroxyl groups of the ACP adsorbent and basic sites at *tri*–bonded (N) atoms, and di–bonded (S) atom in MB adsorbent.

The domination and participation of each interaction is based on the characteristic of each ACP materials and the formation parameters in terms of impregnation acid ratio and activation temperature.

Finally, the performance of the formed ACP adsorbent materials can be judged by comparison of (i) the surface area and (ii) MB adsorption capacity for the present ACP materials with some recently reported materials, as shown in Table 5. Thus, high surface area values, as well as, exceptionally high adsorptive capacity results can be recognized for the present ACP materials. This confirms that ACP materials are benefit from the effect of phosphoric acid in developing oxygenated (P) sites, oxidized (C) sites as well as development of slit-shaped porosity throughout the thermochemical activation. This process occurred via replacing the less stable groups with the formation of more stable (C–O–P) groups that retard heat shrinking effect and protect the porous texture against collapse at high temperature. It should be emphasized that the chemical composition and structural nature of OP were assisted the effect of phosphoric acid to take place and facilitated the formation of the indicated plate-like mesoporous particles of graphene like structure.

4. Conclusions

The above results demonstrate that high quality P-doped activated carbons, ACP, were obtained from orange peel as a soft lignocellulose material. The effect of P-doping and thermal activation were assisted the formation of stabilized nanoporous texture with improved adsorption behaviors towards methylene blue.

Thus, the following conclusions can be made:

- P-containg activated carbons (ACP)s with high carbon contents were formed by activation of orange peel biomass materials with phosphoric acid through the dehydration, polymerization and restructuring. Due to the nature of the orange peel biomass material, and the action of H_3PO_4, nanostructured graphene−like layers were formed.
- Increasing of P-doping ratio (H_3PO_4 impregnation ratio) and activation temperature assisted porous texture stability against collapse and substantially limits the formation of unstable bulky functional groups at high activation temperature.
- P-doping led to preservation of high surface area and improves formation of thermally stable nanostructured graphene-like layers and plate like amorphous graphite particles with limited number of graphene layers (each particle composed of few graphene layers).
- The adsorption isotherms if MB showed monolayer adsorption behavior for ACP materials obtained at high acid ratios and high activation temperatures, which indicates formation of more active sites that led to high adsorption capacity.
- The proposed adsorption mechanism give insight into the effect of P-doping and textural improvement to the adsorption behavior which based on electrostatic interaction and hydrogen bonding.

Table 5
The comparison between specific surface, S_{BET}, area and methylene blue adsorption capacity, q_{max}, of some reported activated carbons with the present OP derived ACP adsorbent materials.

Raw material	Biomass activation (*act*) conditions	MB adsorption (*ads*) conditions	Surface area	Adsorption capacity	Reference
	Reagent (*Re*), *Re*: Biomass (*Ratio*), Temp of *act* (Tact), Atmosphere (*At*) Time of *act* (*t*.a)	MB conc = [MB], pH of *ads* (pH), Temp of *ads* (Tads), Mass of adsorbent (*m*), time of contact (*t*.c)	S_{BET} (m^2/g)	q_{max} (mg/g)	
Rice straw	Re= $ZnCl_2$ Ratio = 1/5 w/w Tact = 700 °C. At= N_2 (250 cm^3/min) t.a = 1 h	[MB] = 2–12 mg/L, pH = 7 Tads = 25 °C, m = 2 mg/100 mL MB soln *t*.c = 24 h	942.7	399	[86]
Litsea glutinosa seeds	Re= $NaHCO_3$ Ratio = 0.1 M Tact = 300–500 °C At= NA; *t*.a = 15–75 mint	[MB] = 10–200 mg/L pH = 3–11 Tads = 25–50 °C, m = 4–12 g/L *t*.c = 24 h	33.16	29.03	[87]
Rattan Furniture	Re= NaOH Ratio = 3:1 (w/w) Tact = 600 °C At= N_2 (150 cm^3/min) *t*.a = 1 h	[MB] = 25 mg/L, pH = 7 Tads = 30 °C m = 0.20 g *t*.c = 8 h	1135	359	[88]
Pineapple	Re= $ZnCl_2$ Ratio = 1:1 (w/w) Tact = 500 °C At= N_2 (150 cm^3/min) *t*.a = 1 h	[MB] = 5–400 mg/L pH = 7 Tads = 30 °C, m = 0.1–5.0 g *t*.c = 12h	914.67	288.34	[89]
Date pits	Re= $FeCL_3$ Ratio = NA Tact = 700 °C At = NA t.a = 1 h	[MB] = 50–450 mg/L pH = 7 Tads = 303–323 K m = 0.02 g *t*.c = 4.5 h	780.06	259.25	[90]
Orange peel	Re= H_3PO_4 Ratio = 1: 2; 1: 1; and 2: 1 (w/w). Tact = 400 –800 °C At= N_2 (150 cm^3/min) *t*.a = 1 h	[MB] = 50–800 mg/L pH = 6.5 Tads = 25 ± 1 °C M = 100 mg/50 mL, t.c = 3h	1204–1706	384–452	This work
DOC-AC	Re= K_2CO_3 Ratio =1.0 –5.0(w/w) Tact = 600–800 °C At = N_2 (100 ml/min) *t*.a = 60-120 min	[MB] = 25–400 mg/L pH = 3–11 Tads = 30–50 °C M = 0.20 g, *t*.c = 0–26 h	988.75	359.38	[74]
Sterculia foetida	Re = H_3PO_4 Ratio = 40% (w/v) Tact = 600 °C At = N_2 (150 ml/min) *t*.a = 30–120 mint	[MB] = 50–500 mg/L pH = 2–12 Tads = 298–328 K M = 1–4 g/l t.c = 0–24 h	89.9–302.6	181.81	[84]
Macadamia nutshells	Re= K_2CO_3; H_2SO_4 *Ratio* = 50% (w/w) *T*act = 650 °C *At* = NA *t*.a =0-90 min	[MB] = 70 mg/L pH= 2–12 *T*ads = 298–328 K *m* = 0.2–2 g/L *t*.c = 0–90 min	426.3–459.8	250.2–261.5	[91]

CRediT authorship contribution statement

Kamal M.S. Khalil: Conceptualization, Methodology, Supervision, Writing – review & editing. **Walaa A. Elhamdy:** Investigation, Formal analysis, Data creation, Writing – original draft. **Khaled M.H. Mohammed:** Supervision, Visualization. **Abd-El-Aziz A. Said:** Supervision, Methodology, Visualization.

Declaration of competing interest

The authors declare the following financial interests/personal relationships which may be considered as potential competing interests:

Appendix A. Supplementary data

Supplementary data to this article can be found online at https://doi.org/10.1016/j.matchemphys.2022.125881.

References

[1] D. Chen, Special issue on nanomaterials for adsorptive removal of contaminants from aqueous solutions (Nano-adsorbents), J. Taiwan Inst. Chem. Eng. 112 (2020) 1–3.
[2] Q. Chen, X. Tan, Y. Liu, S. Liu, M. Li, Y. Gu, Biomass-derived porous graphitic carbon materials for energy and environmental applications, J. Mater. Chem. 8 (2020) 5773–5811.
[3] K.M.S. Khalil, O.A.S. Allam, M. Khairy, K.M.H. Mohammed, R.M. Elkhatib, M. A. Hamed, High surface area nanostructured activated carbons derived from sustainable sorghum stalk, J. Mol. Liq. 247 (2017) 386–396.
[4] M. Khairy, A.H. Mahmoud, K.M.S. Khalil, RSC Advances Synthesis of Highly Crystalline LaFeO 3 Nanospheres for Phenoxazinone Synthase Mimicking Activity, 2021, pp. 17746–17754.
[5] K.M.S. Khalil, A.H. Mahmoud, M. Khairy, Formation and textural characterization of size-controlled LaFeO$_3$ perovskite nanoparticles for efficient photocatalytic degradation of organic pollutants, Adv. Powder Technol. 33 (1) (2022) 103429.
[6] Z. Li, D. Franco, M. Schadeck, J. Georgin, Adsorption of Hazardous Dyes on Functionalized Multiwalled Carbon Nanotubes in Single and Binary Systems : Experimental Study and Physicochemical Interpretation of the Adsorption Mechanism, vol. 389, February, 2020.
[7] M. Danish, T. Ahmad, S. Majeed, M. Ahmad, L. Ziyang, Z. Pin, S.M.S. Iqbal, Bioresource Technology Reports Use of banana trunk waste as activated carbon in scavenging methylene blue dye : kinetic , thermodynamic , and isotherm studies, Bioresour. Technol. Reports 3 (August) (2018) 127–137.
[8] X. Pang, D. Franco, G. Luiz, J. Georgin, Adsorption of crystal violet on biomasses from pecan nutshell , para chestnut husk, araucaria bark. palm cact. : Experiment. study theor. model. via monol. double layer statist. phy. model. 378 (2019). June.
[9] B.S. Marques, T.S. Frantz, T. Roberto, S. Anna, C. Junior, L. Antonio, D.A. Pinto, G. L. Dotto, B.S. Marques, Adsorption of a textile dye onto piaçava fibers : kinetic , equilibrium , thermodynamics , and application in simulated effluents, Environ. Sci. Pollut. Res. 26 (2019) 28584–28592.
[10] S. Xu, W. Yu, S. Liu, C. Xu, J. Li, Y. Zhang, Adsorption of hexavalent chromium using banana pseudostem biochar and its mechanism, Sustain. Times 10 (11) (2018).
[11] S. Hashemian, K. Salari, Z.A. Yazdi, Preparation of activated carbon from agricultural wastes (almond shell and orange peel) for adsorption of 2-pic from aqueous solution, J. Ind. Eng. Chem. 20 (4) (2014) 1892–1900.
[12] M. Wu, Q. Guo, G. Fu, Preparation and characteristics of medicinal activated carbon powders by CO2 activation of peanut shells, Powder Technol. 247 (2013) 188–196.
[13] L.A. da Silva, S.M.S. Borges, P.N. Paulino, M.A. Fraga, S.T. de Oliva, S.G. Marchetti, M. do C. Rangel, Methylene blue oxidation over iron oxide supported on activated carbon derived from peanut hulls, Catal. Today 289 (2017) 237–248.
[14] G. da C. Gonçalves, N.C. Pereira, M.T. Veit, Production of bio-oil and activated carbon from sugarcane bagasse and molasses, Biomass Bioenergy 85 (2016) 178–186.
[15] A. Shakya, T. Agarwal, Removal of Cr(VI) from water using pineapple peel derived biochars: adsorption potential and re-usability assessment, J. Mol. Liq. 293 (2019) 111497.
[16] A.M. Aldawsari, I. Alsohaimi, H.M.A. Hassan, Z.E.A. Abdalla, I. Hassan, M. R. Berber, Tailoring an efficient nanocomposite of activated carbon-layered double hydroxide for elimination of water-soluble dyes, J. Alloys Compd. 857 (2021) 157551.
[17] K. Gupta, D. Gupta, O.P. Khatri, Graphene-like porous carbon nanostructure from Bengal gram bean husk and its application for fast and efficient adsorption of organic dyes, Appl. Surf. Sci. 476 (2019) 647–657, no. December 2018.
[18] J.P. Paraknowitsch, A. Thomas, Doping carbons beyond nitrogen: an overview of advanced heteroatom doped carbons with boron, sulphur and phosphorus for energy applications, Energy Environ. Sci. 6 (10) (2013) 2839–2855.
[19] S. Gaspard, N. Passe, Activated Carbon from Biomass for Water Treatment, vol. 25, 2014.
[20] S. Román, J.M. Valente Nabais, B. Ledesma, J.F. González, C. Laginhas, M. M. Titirici, Production of low-cost adsorbents with tunable surface chemistry by conjunction of hydrothermal carbonization and activation processes, Microporous Mesoporous Mater. 165 (2013) 127–133.
[21] D. Hulicova-Jurcakova, A.M. Puziy, O.I. Poddubnaya, F. Suárez-García, J.M. D. Tascón, G.Q. Lu, Highly stable performance of supercapacitors from phosphorus-enriched carbons, J. Am. Chem. Soc. 131 (14) (Apr. 2009) 5026–5027.
[22] W. Ma, L. Xie, L. Dai, G. Sun, J. Chen, F. Su, Y. Cao, H. Lei, Q. Kong, C.-M. Chen, Influence of phosphorus doping on surface chemistry and capacitive behaviors of porous carbon electrode, Electrochim. Acta 266 (2018) 420–430.
[23] A. Guediri, A. Bouguettoucha, D. Chebli, N. Chafai, A. Amrane, Molecular dynamic simulation and DFT computational studies on the adsorption performances of methylene blue in aqueous solutions by orange peel-modified phosphoric acid, J. Mol. Struct. 1202 (2020) 127290.
[24] S.S. Lam, R.K. Liew, Y.M. Wong, P.N.Y. Yek, N.L. Ma, C.L. Lee, H.A. Chase, Microwave-assisted pyrolysis with chemical activation, an innovative method to convert orange peel into activated carbon with improved properties as dye adsorbent, J. Clean. Prod. 162 (2017) 1376–1387.
[25] M.E. Fernandez, G.V. Nunell, P.R. Bonelli, A.L. Cukierman, Activated carbon developed from orange peels: batch and dynamic competitive adsorption of basic dyes, Ind. Crop. Prod. 62 (2014) 437–445.
[26] A. Pandiarajan, R. Kamaraj, S. Vasudevan, S. Vasudevan, OPAC (orange peel activated carbon) derived from waste orange peel for the adsorption of chlorophenoxyacetic acid herbicides from water: adsorption isotherm, kinetic modelling and thermodynamic studies, Bioresour. Technol. 261 (April) (2018) 329–341.
[27] J. Li, H. Bai, X. Li, W. Li, J. Zhai, M. Li, G. Xi, Hierarchical porous carbon microspheres with superhydrophilic surface for efficient adsorption and detection of water-soluble contaminants, J. Mater. Chem. 6 (25) (2018) 12153–12161.
[28] F. Ding, J. Li, H. Du, J. Zhao, K. Qu, Y. Li, X. Zhang, Y. Zhang, Y. Qin, W. Lu, Highly porous heteroatom doped-carbon derived from orange peel as electrode materials for high-performance supercapacitors, Int. J. Electrochem. Sci. 15 (2020) 5632–5649.
[29] M. Dhelipan, A. Arunchander, A.K. Sahu, D. Kalpana, Activated carbon from orange peels as supercapacitor electrode and catalyst support for oxygen reduction reaction in proton exchange membrane fuel cell, J. Saudi Chem. Soc. 21 (4) (2017) 487–494.
[30] H. Shen, X. Xia, Y. Ouyang, X. Jiao, S. Mutahir, D. Mandler, Q. Hao, Preparation of biomass-based porous carbons with high specific capacitance for applications in supercapacitors, Chemelectrochem 6 (14) (2019) 3599–3605.
[31] S. Ahmed, M. Rafat, A. Ahmed, Nitrogen doped activated carbon derived from orange peel for supercapacitor application, Adv. Nat. Sci. Nanosci. Nanotechnol. 9 (3) (2018).
[32] K. Subramani, N. Sudhan, M. Karnan, M. Sathish, Orange peel derived activated carbon for fabrication of high-energy and high-rate supercapacitors, ChemistrySelect 2 (35) (2017) 11384–11392.
[33] J.J. Manyà, Pyrolysis for biochar purposes: a review to establish current knowledge gaps and research needs, Environ. Sci. Technol. 46 (15) (Aug. 2012) 7939–7954.
[34] Kamal M.S. Khalil, Walaa A. Elhamdy, Ahmed A. Elsamahy, Biomass derived P-doped activated carbon as nanostructured mesoporous adsorbent for chromium (VI) pollutants with pronounced functional efficiency and recyclability, Colloids and Surfaces A: Physicochemical and Engineering Aspects 641 (2022) 128553 641 (2022) 128553, https://doi.org/10.1016/j.colsurfa.2022.128553.
[35] Https://www.selinawamucii.com/produce/fruits-and-vegetables/egypt-oranges/, “Fruits and Vegetables.”.
[36] K.M.S. Khalil, W.A. Elhamdy, M.N. Goda, A.-E.-A.A. Said, Biomass derived P-containing activated carbons as a novel green catalyst/support for methanol conversion to dimethyl ether alternative fuel, J. Environ. Chem. Eng. (2021) 106572.
[37] M.A.P. Cechinel, S.M.A.G. Ulson De Souza, A.A. Ulson De Souza, Study of lead (II) adsorption onto activated carbon originating from cow bone, J. Clean. Prod. 65 (2014) 342–349.
[38] S. Lagergren, Zur theorie der sogenannten adsorption geloster stoffe, K. - Sven. Vetenskapsakademiens Handl. 24 (1898) 1–39.
[39] Y.S. Ho, G. McKay, Sorption of dye from aqueous solution by peat, Chem. Eng. J. 70 (2) (1998) 115–124.
[40] Y.S. Ho, G. McKay, Comparative sorption kinetic studies of dye and aromatic compounds onto fly ash, J. Environ. Sci. Heal. - Part A Toxic/Hazardous Subst. Environ. Eng. 34 (5) (1999) 1179–1204.
[41] Z. Yang, Z. Zhao, X. Yang, Z. Ren, Xanthate modified magnetic activated carbon for efficient removal of cationic dyes and tetracycline hydrochloride from aqueous solutions, Colloids Surfaces A Physicochem. Eng. Asp. 615 (2021) 126273, no. December 2020.
[42] J. Bedia, R. Barrionuevo, J. Rodríguez-Mirasol, T. Cordero, Ethanol dehydration to ethylene on acid carbon catalysts, Appl. Catal. B Environ. 103 (3–4) (2011) 302–310.
[43] F. Rodríguez-Reinoso, M. Molina-Sabio, Activated carbons from lignocellulosic materials by chemical and/or physical activation: an overview, Carbon N. Y. 30 (7) (1992) 1111–1118.
[44] M. Jagtoyen, F. Derbyshire, Activated carbons from yellow poplar and white oak by H3PO4 activation, Carbon N. Y. 36 (7) (1998) 1085–1097.
[45] 2009 JCPDS, International Centre for Diffraction Data, PCPDFWIN, JCPDS-ICDD, “International Centre for Diffraction Data, PCPDFWIN, JCPDS-ICDD, 2009, 2009.
[46] S. Drewniak, R. Muzyka, A. Stolarczyk, T. Pustelny, M. Kotyczka-Morańska, M. Setkiewicz, Studies of reduced graphene oxide and graphite oxide in the aspect of their possible application in gas sensors, Sensors 16 (1) (2016).

[47] K. Krishnamoorthy, M. Veerapandian, K. Yun, S.J. Kim, The chemical and structural analysis of graphene oxide with different degrees of oxidation, Carbon N. Y. 53 (2013) 38–49.

[48] L. Shen, L. Zhang, K. Wang, L. Miao, Q. Lan, K. Jiang, H. Lu, M. Li, Y. Li, B. Shen, W. Zheng, Analysis of oxidation degree of graphite oxide and chemical structure of corresponding reduced graphite oxide by selecting different-sized original graphite, RSC Adv. 8 (31) (2018) 17209–17217.

[49] X. Zhu, Y. Liu, G. Luo, F. Qian, S. Zhang, J. Chen, Facile fabrication of magnetic carbon composites from hydrochar via simultaneous activation and magnetization for triclosan adsorption, Environ. Sci. Technol. 48 (10) (May 2014) 5840–5848.

[50] L.M. Malard, M.A. Pimenta, G. Dresselhaus, M.S. Dresselhaus, Raman spectroscopy in graphene, Phys. Rep. 473 (5) (2009) 51–87.

[51] J.J. Morgan, M.F. Craciun, S.J. Eichhorn, Quantification of stress transfer in a model cellulose nanocrystal/graphene bilayer using Raman spectroscopy, Compos. Sci. Technol. 177 (2019) 34–40.

[52] A.M. Puziy, O.I. Poddubnaya, A. Martínez-Alonso, F. Suárez-García, J.M.D. Tascón, Surface chemistry of phosphorus-containing carbons of lignocellulosic origin, Carbon N. Y. 43 (14) (2005) 2857–2868.

[53] A.M. Puziy, O.I. Poddubnaya, A. Martínez-Alonso, A. Castro-Muñiz, F. Suárez-García, J.M.D. Tascón, Oxygen and phosphorus enriched carbons from lignocellulosic material, Carbon N. Y. 45 (10) (2007) 1941–1950.

[54] E. Fuente, J.A. Menéndez, M.A. Díez, D. Suárez, M.A. Montes-Morán, Infrared spectroscopy of carbon materials: a quantum chemical study of model compounds, J. Phys. Chem. B 107 (26) (Jul. 2003) 6350–6359.

[55] M.S. Solum, R.J. Pugmire, M. Jagtoyen, F. Derbyshire, Evolution of carbon structure in chemically activated wood, Carbon N. Y. 33 (9) (1995) 1247–1254.

[56] Q. Miao, Y. Tang, J. Xu, X. Liu, L. Xiao, Q. Chen, Activated carbon prepared from soybean straw for phenol adsorption, J. Taiwan Inst. Chem. Eng. 44 (3) (2013) 458–465.

[57] M. Danish, R. Hashim, M.N.M. Ibrahim, O. Sulaiman, Optimized preparation for large surface area activated carbon from date (Phoenix dactylifera L.) stone biomass, Biomass Bioenergy 61 (2014) 167–178.

[58] J. Xu, L. Chen, H. Qu, Y. Jiao, J. Xie, G. Xing, Preparation and characterization of activated carbon from reedy grass leaves by chemical activation with H3PO4, Appl. Surf. Sci. 320 (2014) 674–680.

[59] R.G. Pereira, C.M. Veloso, N.M. [da Silva], L.F. [de Sousa], R.C.F. Bonomo, A. O. [de Souza], M.O. da Guarda Souza, R. da Costa Ilhéu Fontan, Preparation of activated carbons from cocoa shells and siriguela seeds using H3PO4 and ZnCL2 as activating agents for BSA and α-lactalbumin adsorption, Fuel Process. Technol. 126 (2014) 476–486.

[60] M. Nahil, P. Williams, Pore characteristics of activated carbons from the phosphoric acid chemical activation of cotton stalks, Biomass Bioenergy 37 (Feb. 2012) 142–149.

[61] V. Fierro, V. Torne, D. Montané, A. Celzard, Study of the decomposition of Kraft lignin impregnated with orthophosphoric acid, Thermochim. Acta 433 (Aug. 2005) 142–148.

[62] I. [Ahmed Hared], J.-L. Dirion, S. Salvador, M. Lacroix, S. Rio, Pyrolysis of wood impregnated with phosphoric acid for the production of activated carbon: kinetics and porosity development studies, J. Anal. Appl. Pyrolysis 79 (1) (2007) 101–105.

[63] M. Olivares-Marín, C. Fernández-González, A. Macías-García, V. Gómez-Serrano, Thermal behaviour of lignocellulosic material in the presence of phosphoric acid. Influence of the acid content in the initial solution, Carbon N. Y. 44 (11) (2006) 2347–2350.

[64] A. Bin Noor, M. Asri, B. Mohd, Textural characteristics of activated carbons prepared from oil palm shells activated with ZnCl 2 and pyrolysis under nitrogen and carbon dioxide, J. Phys. Sci. 19 (2) (2008) 93–104.

[65] D. Prahas, Y. Kartika, N. Indraswati, S. Ismadji, Activated carbon from jackfruit peel waste by H3PO4 chemical activation: pore structure and surface chemistry characterization, Chem. Eng. J. 140 (1–3) (2008) 32–42.

[66] K.C. Bedin, I.P.A.F. Souza, A.L. Cazetta, L. Spessato, A. Ronix, V.C. Almeida, CO2-spherical activated carbon as a new adsorbent for Methylene Blue removal: kinetic, equilibrium and thermodynamic studies, J. Mol. Liq. 269 (2018) 132–139.

[67] C.H. Giles, D. Smith, A. Huitson, A general treatment and classification of the solute adsorption isotherm. I. Theoretical, J. Colloid Interface Sci. 47 (3) (1974) 755–765.

[68] C.H. Giles, A.P. D'Silva, I.A. Easton, A general treatment and classification of the solute adsorption isotherm part. II. Experimental interpretation, J. Colloid Interface Sci. 47 (3) (1974) 766–778.

[69] I. Langmuir, The adsorption of gases on plane surface of Glass,Mica and platinum, Res. Lab. Gen. Electr. Co. 2009 (1918) 1361–1402.

[70] E. Darstellung, H. Freundlich, der chemie der kolloide und verwanter gebiete, A. Bibliotek, "AcademisheBibliotek," 1909, 1909.

[71] M.J. Tempkin, V. Pyzhev, Recent modifications to Langmuir isotherms,, Acta Physiochem. USSR, 12 (1940) 217–225.

[72] M.M. Dubinin, L.V. Radushkevich, Equation of the characteristic curve of activated charcoal, Proc. Acad. Sci. USSR Phys. Chem. Sect 55 (1947) 331–333.

[73] W. Li, H. Wei, Y. Liu, S. Li, G. Wang, H. Han, Fabrication of novel starch-based composite hydrogel microspheres combining Diels-Alder reaction with spray drying for MB adsorption, J. Environ. Chem. Eng. 9 (5) (2021) 105929.

[74] F. Marrakchi, B.H. Hameed, M. Bouaziz, Mesoporous and high-surface-Area activated carbon from defatted olive cake by-products of olive mills for the adsorption kinetics and isotherm of methylene blue and acid blue 29, J. Environ. Chem. Eng. 8 (5) (2020) 104199.

[75] D.I. Mendoza-castillo, H.E.R. ávila (Eds.), Adsorption Processes for Water Treatment and Puri Cation, 2017.

[76] Z.A. Al-Othman, M.A. Habila, R. Ali, M.S.E.D. Hassouna, Kinetic and thermodynamic studies for methylene blue adsorption using activated carbon prepared from agricultural and municipal solid wastes, Asian J. Chem. 25 (15) (2013) 8301–8306.

[77] N.M. Mahmoodi, Equilibrium, kinetics, and thermodynamics of dye removal using alginate in binary systems, J. Chem. Eng. Data 56 (6) (Jun. 2011) 2802–2811.

[78] A.M. Aljeboree, A.F. Alkaim, A.H. Al-Dujaili, Adsorption isotherm, kinetic modeling and thermodynamics of crystal violet dye on coconut husk-based activated carbon, Desalination Water Treat. 53 (13) (2015) 3656–3667.

[79] S. Chakraborty, S. Chowdhury, P. Das Saha, Adsorption of Crystal Violet from aqueous solution onto NaOH-modified rice husk, Carbohydr. Polym. 86 (4) (2011) 1533–1541.

[80] A.M.M. Vargas, A.L. Cazetta, M.H. Kunita, T.L. Silva, V.C. Almeida, Adsorption of methylene blue on activated carbon produced from flamboyant pods (Delonix regia): study of adsorption isotherms and kinetic models, Chem. Eng. J. 168 (2) (2011) 722–730.

[81] O.V. Ovchinnikov, A.V. Evtukhova, T.S. Kondratenko, M.S. Smirnov, V. Y. Khokhlov, O.V. Erina, Manifestation of intermolecular interactions in FTIR spectra of methylene blue molecules, Vib. Spectrosc. 86 (2016) 181–189.

[82] M. Auta, B.H. Hameed, Chitosan–clay composite as highly effective and low-cost adsorbent for batch and fixed-bed adsorption of methylene blue, Chem. Eng. J. 237 (2014) 352–361.

[83] M. Doğan, H. Abak, M. Alkan, Adsorption of methylene blue onto hazelnut shell: kinetics, mechanism and activation parameters, J. Hazard Mater. 164 (1) (2009) 172–181.

[84] S. Basu, G. Ghosh, S. Saha, Adsorption characteristics of phosphoric acid induced activation of bio-carbon: equilibrium, kinetics, thermodynamics and batch adsorber design, Process Saf. Environ. Protect. 117 (2018) 125–142.

[85] M. Doğan, M. Alkan, Ö. Demirbaş, Y. Özdemir, C. Özmetin, Adsorption kinetics of maxilon blue GRL onto sepiolite from aqueous solutions, Chem. Eng. J. 124 (1–3) (2006) 89–101.

[86] S. Sangon, A.J. Hunt, Y. Ngernyen, S. Youngme, N. Supanchaiyamat, Rice straw-derived highly mesoporous carbon-zinc oxide nanocomposites as high performance photocatalytic adsorbents for toxic dyes, J. Clean. Prod. 318 (2021) 128583. July.

[87] M. Uyen, H. Sinh, H.Y. Hoang, V. Anh, V.D. Doan, Natural core-shell structure activated carbon beads derived from Litsea glutinosa seeds for removal of methylene blue : facile preparation , characterization , and adsorption properties, Environ. Res. 198 (2021) 110481. September 2020.

[88] M.A. Islam, M.J. Ahmed, W.A. Khanday, M. Asif, B.H. Hameed, Mesoporous activated carbon prepared from NaOH activation of rattan (Lacosperma secundiflorum) hydrochar for methylene blue removal, Ecotoxicol. Environ. Saf. 138 (Apr. 2017) 279–285.

[89] M.N. Mahamad, M.A.A. Zaini, Z.A. Zakaria, Preparation and characterization of activated carbon from pineapple waste biomass for dye removal, Int. Biodeterior. Biodegrad. 102 (2015) 274–280.

[90] S.K. Theydan, M.J. Ahmed, Adsorption of methylene blue onto biomass-based activated carbon by FeCl3 activation: equilibrium, kinetics, and thermodynamic studies, J. Anal. Appl. Pyrolysis 97 (2012) 116–122.

[91] T.M. Dao, T. Le Luu, Synthesis of activated carbon from macadamia nutshells activated by H2SO4 and K2CO3 for methylene blue removal in water, Bioresour. Technol. Reports 12 (2020) 100583.